

Mixed enrichment for the finite element method in heterogeneous media

G.C. Diwan¹, M.S. Mohamed², M. Seaid¹, J. Trevelyan¹ and O. Laghrouche²

¹ School of Engineering and Computing Sciences, University of Durham, South Road, Durham DH1 3LE, UK

² Institute for Infrastructure and Environment, Heriot Watt University, Riccarton, Edinburgh EH14 4AS, UK

Abstract

Problems of multiple scales of interest or of locally nonsmooth solutions may often involve heterogeneous media. These problems are usually very demanding in terms of computations with the conventional finite element method. On the other hand different enriched finite element methods such as the partition of unity which proved to be very successful in treating similar problems, are developed and studied for homogeneous media. In this work we present a new idea to extend the partition of unity finite element method to treat heterogeneous materials. The idea is studied in applications to wave scattering and heat transfer problems where significant advantages are noted over the standard finite element method. Although presented within the partition of unity context the same enrichment idea can also be extended to other enriched methods to deal with heterogeneous materials.

Keywords. Finite element method; Partition of unity method; acoustic wave scattering, Transient heat transfer; Composite materials; heterogeneous media; multiscale

1 Introduction

Numerical modelling of natural phenomena or industrial processes that involve multiple scales of interest, have a wide range of applications of fundamental and practical importance. Such applications are often encountered in problems in heterogeneous media. Transport processes in porous or disordered media [20, 5], biomedicine [28] and remote sensing [36] are a few to name. For example in a remote sensing problem [4] the spatial domain can be of many orders or magnitude larger than the propagating wave length. Solving this problem with the standard Finite Element Method (FEM) usually requires many nodal points per wavelength in order to recover the solution with a reasonable engineering accuracy. Thus the solution can be very demanding in terms of the computational resources not only because of the domain size but also because of the discontinuities in the physical properties due to the problem heterogeneity. Furthermore, local irregularities such as singularities or steep gradients in the solution at the vicinity of the fibres or particles in a composite material, can have an extra impact on the efficiency and the robustness of the solution [35]. It can even result in a numerical bottleneck especially in the time domain.

In a homogeneous media it was proved that enriching the finite element solution space with special functions can be efficient in dealing with difficulties related to multiscale problems or local irregularities [16, 26]. For example plane waves are used in several enrichment approaches to reduce the computational costs of modelling wave problems. The approaches include: the Partition of

Unity Finite Element Method (PUFEM) [12, 14], the generalized finite element method [30, 31], the partition of unity boundary element method [23, 15], the ultraweak variational formulation [2, 11] and the discontinuous enrichment method [32, 8]. In all these cases the solution space is enriched with wave-like functions in order to circumvent the need for highly refined meshes due to short waves propagating in the problem domain. Similarly in heat transfer problems to overcome difficulties related to thermal gradients Van der Meer *et al.* [34] developed a set of algorithms to study transient geothermal problems using time-dependent enrichment to approximate the solution. Hence, the evolution of thermal gradients with time is considered by updating the enrichment so that it remains optimal at each time step. O'Hara *et al.* [21] applied global-local enrichment to transient problems with highly localized sharp thermal gradients using the generalized finite element method [22]. More recently Mohamed *et al.* [26] presented a finite element solution for transient diffusion problems enriched by a family of Gaussian functions. The temporal behaviour of the problem was considered using multiple time-independent enrichment functions giving rise to much improved computational efficiency since the same system matrix could be used at each time step. This work was extended later to consider radiative heat transfer in a grey material [27] and in glass cooling [18] where a q -refinement procedure is presented to deal with radiation rates at multiple frequency bands.

It was until recently that enriched approaches were investigated for heat transfer in heterogeneous media. To express discontinuous gradient fields with thermal problems Soghrati *et al.* [29] enriched a finite element approximation, using combinations of Lagrangian shape functions. In a different work Yu and Gong [37] adopted an eXtended finite element method to avoid mesh dependency on the material interfaces. The cross element discontinuity is modelled using a modified level set enrichment function. In both references [29] and [37] the enrichment is used to allow material interfaces to pass through elements, and weak discontinuities at these interfaces are captured. However, fine meshes will still be required to capture high thermal gradients. On the other hand several authors have developed enrichment approaches to model wave scattering in a heterogeneous medium. Different contributions have been made to this type of problem using the concept of the partition of unity method [16]. Laghrouche *et al.* [13] used specific enrichment for each subdomain constituting the composite media. Continuity between subdomains is ensured with Lagrange multipliers. A recent contribution is found in [6] where Facco *et al.* used a partition of unity method based mortar finite element method to solve the scattering of transverse electromagnetic wave. The method uses the idea of mortar elements, where, the continuity between two domains is achieved by directly coupling the corresponding basis functions of the nodes on the interface. This has been shown to result into a positive definite linear system and thus efficient iterative solvers can be employed. A more relevant contribution is due to Chazot *et al.* [3] where Lagrange multipliers are used to couple two medium namely air and a porous absorbing material to solve the Helmholtz equation with the PUFEM. In a very recent work Tezaur *et al.* [25] extended the concept of the discontinuous enrichment method [7] into problems of a spatially variable wavenumber.

Due to the different physical properties of the materials composing a heterogeneous media, it is important to define the enrichment based on each material/subdomain. This results in several enrichment functions that need to be continuous in between these subdomains. In this work we propose to combine these functions by applying each one over the entire domain such that the resulting enrichment is a hybrid of these functions. This strategy does not result in discontinuities such as in [13, 3, 25]. Compared to the previous works, in this paper there is no need to use Lagrange multipliers which are known to result into a linear system that is not positive definite [24]. Besides rendering a non-positive definite structure (presence of zeros on the diagonal of the associated matrices) of the linear system, the use of Lagrange multipliers results into additional unknowns and increases the bandwidth of the system matrix. Also, the equations in the linear system need to be arranged carefully to avoid the problems when solving the system with direct solvers such as Gauss elimination. Furthermore, as the number of subdomains increases a significant computational

cost arises in order to handle the boundary integrals resulting from the coupling conditions at the interfaces. On the other hand the proposed hybrid enrichment can satisfactorily deal with all these subdomains without disturbing the continuity. The proposed strategy is tested in two different applications namely wave scattering and transient heat transfer in heterogeneous media.

The remainder of the paper is organized as follows. In Section 2 we briefly state the governing equations for the problems studied here. Then, we introduce the ingredients of the PUFEM and its implementation in Section 3 where the finite element discretization of the space and enrichment functions are presented as well. Section 4 shows the results for our numerical applications in wave scattering for two- and four-layered medium and then in the transient heat transfer in composites of two and three materials. The presented results clearly show the overall efficiency of the proposed PUFEM compared to the polynomial based finite element. Finally, we conclude with some remarks in Section 5.

2 Model problem

Second-order partial differential equations appear in many subjects such as wave scattering, diffusion process, simulation of heat conduction, and groundwater flows. Second-order partial differential equations can also be used to model water waves in shallow water flows. In the current work, we consider a class of second-order partial differential equations written in the generic form

$$\alpha(\mathbf{x})U + \nabla \cdot (\mathcal{K}(\mathbf{x})\nabla U) = F, \quad \mathbf{x} \in \Omega, \quad (1a)$$

$$\beta(\hat{\mathbf{x}})U + \mathcal{K}(\hat{\mathbf{x}})\mathbf{n}(\hat{\mathbf{x}}) \cdot \nabla U = f, \quad \hat{\mathbf{x}} \in \Gamma, \quad (1b)$$

where \mathbf{x} is the spatial point, $U(\mathbf{x})$ is the unknown solution, F and f are source terms, α , \mathcal{K} and β are known coefficients which may depend on \mathbf{x} . The equations (1) have to be solved in a bounded spatial domain Ω in \mathbb{R}^d ($d = 1, 2$ or 3) with a boundary Γ and $\mathbf{n}(\hat{\mathbf{x}})$ denotes the unit outward normal at $\hat{\mathbf{x}}$ with respect to Γ .

In this paper, the emphasis is on second-order partial differential equations raised in modeling acoustic waves and heat transfer. More precisely, the numerical techniques developed here are used to solve:

1. Wave scattering: Starting from the two-dimensional wave equation and assuming a steady state solution, the considered problem is reduced to the following Helmholtz equation

$$\rho \nabla \cdot \left(\frac{1}{\rho} \nabla \phi \right) + k^2(\mathbf{x})\phi = 0 \quad \mathbf{x} \in \Omega, \quad (2)$$

where ϕ is the total acoustic pressure in Ω and $k(\mathbf{x})$ is the wavenumber of the medium at \mathbf{x} . It is clear that the Helmholtz equation (2) can be reformulated in the compact form (1) where $\alpha(\mathbf{x}) = \frac{k^2}{\rho}$, $\mathcal{K}(\mathbf{x}) = \frac{1}{\rho}$ and $F = 0$. In the present study we consider the problem of a plane wave scattering in a heterogeneous media with a jump in the wavenumber as depicted in Figure 1. It should be noted that the jump in the wavenumber arises on account of a discontinuity in the density ρ of the medium. The plane wave $\phi^{\text{inc}}(\mathbf{x}) = e^{i\mathbf{k}\mathbf{d}\cdot\mathbf{x}}$ travelling in the direction \mathbf{d} and being scattered from a circular scatterer in a media with a jump in the wavenumber where $i = \sqrt{-1}$. The computational domain is defined as $\Omega = \Omega_1 \cup \Omega_2$ with Γ_s of radius r_1 is the boundary of the circular cylinder, Γ_{int} of radius r_2 is the interface between the regions Ω_1 and Ω_2 and Γ_r of radius r_3 is an artificial circular truncation boundary. We denote by k_1 and k_2 the wavenumbers in the regions Ω_1 and Ω_2 , respectively. In Figure 1, Ω_∞ is the homogeneous and unbounded domain with wavenumber k_2 , thus, $k_\infty = k_2$. Let ϕ_1 and ϕ_2 denote the total acoustic pressures respectively in the domains Ω_1 and Ω_2 . The scatterer is assumed to be fully rigid, thus, on Γ_s we have

$$\mathbf{n}(\hat{\mathbf{x}}) \cdot \nabla \phi_1 = 0, \quad \hat{\mathbf{x}} \in \Gamma_s,$$

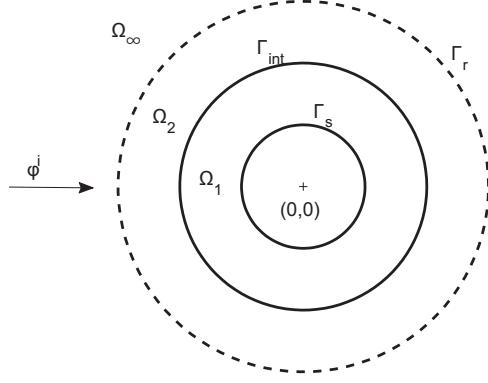


Figure 1: Wave scattering in a medium with jumps in the wavenumber.

which implies the total reflection of the incident plane wave off the cylinder surface Γ_s . The normal particle velocity across the interface, Γ_{int} , between the two subdomains must be continuous *i.e.*,

$$\frac{1}{\rho_1} \mathbf{n}(\hat{\mathbf{x}}) \cdot \nabla \phi_1 = \frac{1}{\rho_2} \mathbf{n}(\hat{\mathbf{x}}) \cdot \nabla \phi_2, \quad \hat{\mathbf{x}} \in \Gamma_{int},$$

where ρ_1 and ρ_2 are the densities of the medium in the domains Ω_1 and Ω_2 , respectively. The third boundary condition is for the scattered waves that travel away from the scatterer into the unbounded domain Ω_∞ . The scattered pressure in the homogeneous exterior domain Ω_∞ (denoted by ϕ_2^{sct}) needs to satisfy the Sommerfeld radiation condition [33]

$$\lim_{r \rightarrow \infty} r^{\frac{d-1}{2}} \left(\frac{\partial}{\partial r} - ik_2 \right) \phi_2^{sct} = 0,$$

where r is the distance of a point in Ω from the origin and d is the dimension of the space. It is well known that the Sommerfeld radiation condition is satisfied exactly only at infinity. Therefore, we truncate the infinite domain by introducing an approximate condition over an artificial boundary (denoted by Γ_r). There are numerous options available for choosing the appropriate approximate condition on Γ_r , compare [33] for a brief review. In the present study, we choose the first-order boundary operator due to Bayliss, Gunzburger and Turkel (BGT-1) given as

$$\mathcal{B}_1 = \left(ik_2 - \frac{1}{2r} \right) \phi_2^{sct},$$

and thus the corresponding boundary condition on Γ_r is either

$$\frac{\partial \phi_2^{sct}}{\partial r} = \mathcal{B}_1 \phi_2^{sct},$$

or

$$\frac{\partial \phi_2^{sct}}{\partial r} + \left(\frac{1}{2r} - ik_2 \right) \phi_2^{sct} = 0.$$

Since $\phi_2 = \phi_2^{sct} + \phi_2^{inc}$, one can write

$$\mathbf{n}(\hat{\mathbf{x}}) \cdot \nabla \phi_2 = \mathbf{n}(\hat{\mathbf{x}}) \cdot \nabla \phi_2^{inc} + \left(\frac{1}{2r} - ik_2 \right) \phi_2^{inc} - \left(\frac{1}{2r} - ik_2 \right) \phi_2.$$

Here we have replaced the spatial derivative with respect to r with the normal derivative as for the case of a circular boundary Γ_r centred at origin, r and the normal coincide.

2. Heat transfer:

$$\rho(\mathbf{x})c(\mathbf{x})\frac{\partial T}{\partial t} - \nabla \cdot (\kappa(\mathbf{x})\nabla T) = S(t, \mathbf{x}), \quad (t, \mathbf{x}) \in (0, t_{final}] \times \Omega, \quad (3a)$$

$$\kappa(\hat{\mathbf{x}})\mathbf{n}(\hat{\mathbf{x}}) \cdot \nabla T + \hbar(\hat{\mathbf{x}})T = \hbar(\hat{\mathbf{x}})T_b(\hat{\mathbf{x}}), \quad (t, \hat{\mathbf{x}}) \in (0, t_{final}] \times \Gamma, \quad (3b)$$

$$T(0, \mathbf{x}) = T_0(\mathbf{x}), \quad \mathbf{x} \in \Omega, \quad (3c)$$

where t is the time variable, T the temperature, ρ the density, c the specific heat capacity, κ the thermal conductivity, \hbar the convective heat transfer coefficient and S a heat source term. Note that in general, the thermal properties of the material, ρ , c and κ depend on the spatial location and may also depend on the material temperature. In the current work we consider the linear problem in which ρ , c and κ are piecewise constant in space. Here, $(0, t_{final}]$ is the time interval, T_0 is a given initial temperature distribution which may depend on the spatial position and T_b is a given temperature of the surrounding. The equations (3) are widely accepted as an accurate model for heat conduction in both participating and non-participating media [17]. These equations do not have analytical solutions for arbitrary geometries and their numerical solutions lead to moving fronts due to the steep gradients in the thermal properties of the material and heat sources.

To integrate the equations (3) we divide the time interval into subintervals $[t_n, t_{n+1}]$ with duration $\Delta t = t_{n+1} - t_n$ for $n = 0, 1, \dots$. We use the notation w^n to denote the value of a generic function w at time t_n . We consider a semi-implicit θ -time stepping scheme, in which the semi-discrete formulation of the heat conduction problem (3a) is given by

$$\rho(\mathbf{x})c(\mathbf{x})\frac{T^{n+1} - T^n}{\Delta t} - (1 - \theta)\nabla \cdot (\kappa(\mathbf{x})\nabla T^{n+1}) - \theta\nabla \cdot (\kappa(\mathbf{x})\nabla T^n) = (1 - \theta)S(t_{n+1}, \mathbf{x}) + \theta S(t_n, \mathbf{x}). \quad (4a)$$

On the boundary, the semi-discrete formulation of (3b) is

$$(1 - \theta)\kappa(\hat{\mathbf{x}})\mathbf{n}(\hat{\mathbf{x}}) \cdot \nabla T^{n+1} + \theta\kappa(\hat{\mathbf{x}})\mathbf{n}(\hat{\mathbf{x}}) \cdot \nabla T^n + (1 - \theta)\hbar(\hat{\mathbf{x}})T^{n+1} + \theta\hbar(\hat{\mathbf{x}})T^n = \hbar(\hat{\mathbf{x}})T_b(\hat{\mathbf{x}}), \quad (4b)$$

where the time parameter θ has to be chosen depending on the time integration scheme; by taking $\theta = 0$ the equation (4) is the first-order Backward Euler scheme, whereas the use of $\theta = \frac{1}{2}$ in the equations (4) yields the second-order Crank-Nicolson scheme. Note that the first-order Euler scheme and the second-order Crank-Nicolson scheme are unconditionally stable for linear problems, so that the choice of Δt may be based on accuracy considerations only. We should also point out that, in the solution procedure, only linear systems of algebraic equations have to be solved at each time step to update the temperature T^{n+1} . The semi-discrete problem (4) can be reformulated in the compact form (1) where

$$\alpha(\mathbf{x}) = \frac{\rho(\mathbf{x})c(\mathbf{x})}{\Delta t}, \quad \mathcal{K}(\mathbf{x}) = -(1 - \theta)\kappa(\mathbf{x}), \quad \beta(\hat{\mathbf{x}}) = (1 - \theta)\hbar(\hat{\mathbf{x}}),$$

and

$$\begin{aligned} F &= \alpha T^n + \theta\nabla \cdot (\kappa(\mathbf{x})\nabla T^n) + (1 - \theta)S(t_{n+1}, \mathbf{x}) + \theta S(t_n, \mathbf{x}), \\ f &= \hbar(\hat{\mathbf{x}})T_b(\hat{\mathbf{x}}) - \theta\kappa(\hat{\mathbf{x}})\mathbf{n}(\hat{\mathbf{x}}) \cdot \nabla T^n - \theta\hbar(\hat{\mathbf{x}})T^n. \end{aligned} \quad (5)$$

The starting point for the use of the finite element method is the weak formulation of the corresponding semi-discrete equations (4b). We proceed as in the conventional finite element formulations by

multiplying equation (1a) by a weighting function W and then integrating over Ω . This yields the statement of the problem to be solved in the weak form, *i.e.* find T^{n+1} such that:

$$\int_{\Omega} \left(\mathcal{K} \nabla W \cdot \nabla T^{n+1} + \alpha W T^{n+1} \right) d\mathbf{x} + \oint_{\Gamma} \beta W T^{n+1} d\hat{\mathbf{x}} = \int_{\Omega} W F d\mathbf{x} + \oint_{\Gamma} W f d\hat{\mathbf{x}}, \quad (6)$$

where W is the trial function. Similarly the weak form for the acoustic scattering problem (2) is: find the pressure ϕ such that

$$\begin{aligned} \int_{\Omega} \left(\frac{1}{\rho} \nabla W \cdot \nabla \phi - \frac{1}{\rho} k^2(\mathbf{x}) W \phi \right) d\mathbf{x} + \left(\frac{1}{2r_3} - ik_2 \right) \int_{\Gamma_r} \frac{1}{\rho} W \phi d\hat{\mathbf{x}} = \\ \int_{\Gamma_r} \frac{1}{\rho} W \left(\mathbf{n}(\hat{\mathbf{x}}) \cdot \nabla \phi^{\text{inc}} + \left(\frac{1}{2r_3} - ik_2 \right) \phi^{\text{inc}} \right) d\hat{\mathbf{x}}, \end{aligned} \quad (7)$$

where r_3 is the radius of the artificial truncation boundary Γ_r . Remark that the boundary integral on Γ_s in the weak form vanishes as the cylinder is assumed to be sound hard. In addition, when performing the domain integral for the mass matrix term (second term in the first integral on left hand side of (7)), the wavenumber $k(\mathbf{x}) = k_1$ if the integration point lies in Ω_1 or $k(\mathbf{x}) = k_2$ otherwise. It should also be pointed out that the weak form (7) is similar to the one used in [13] except the inclusion of an additional boundary integral in [13] that takes into account the continuity of normal particle velocity across the interface Γ_{int} which does not appear in (7).

3 Mixed enrichment for the finite element method

In this section we formulate the proposed PUFEM for the numerical solution of the wave scattering and the heat transfer problems. In order to solve the above weak forms with the finite element method we require a discretization of the space domain $\bar{\Omega} = \Omega \cup \Gamma$. To perform this step, we generate a quasi-uniform partition $\Omega_h \subset \bar{\Omega}$ of small elements \mathcal{T}_j such that $\bar{\Omega} = \bigcup_{j=1}^{N_e} \mathcal{T}_j$, where N_e is the number of elements of Ω_h and h is a space discretization parameter. Next, we formulate the finite element solution to U as

$$U \simeq U_h^n(\mathbf{x}) = \sum_{j=1}^{N_d} U_j^n \psi_j(\mathbf{x}), \quad (8)$$

where N_d is the number of solution mesh points in the partition Ω_h . The functions U_j^n are the corresponding nodal values of $U_h^n(\mathbf{x})$. They are defined as $U_j^n = U_h^n(\mathbf{x}_j)$ where $\{\mathbf{x}_j\}_{j=1}^{N_d}$ are the set of solution mesh points in the partition Ω_h . In (8), $\{\psi_j\}_{j=1}^{N_d}$ are the set of global nodal basis functions characterized by the property $\psi_i(\mathbf{x}_j) = \delta_{ij}$ with δ_{ij} denoting the Kronecker symbol. We introduce $\{\mathbf{x}_1, \dots, \mathbf{x}_M\}$ as the set of M nodal points in the element \mathcal{T}_j . Hereafter, unless otherwise stated, the subscripts h and j are used to refer to coefficients associated with the whole mesh Ω_h and a mesh element \mathcal{T}_j , respectively. The approximation space is then defined as

$$\tilde{V}_h^0 = \text{span} \left\{ \psi_h, \quad U_h = \sum_{j=0}^{N_d} U_j \psi_j \right\}.$$

Using the PUFEM [16] it is possible to enrich the solution space with basis functions that have better approximation properties than the conventional polynomial basis functions. The enrichment used for the applications studied here are presented next.

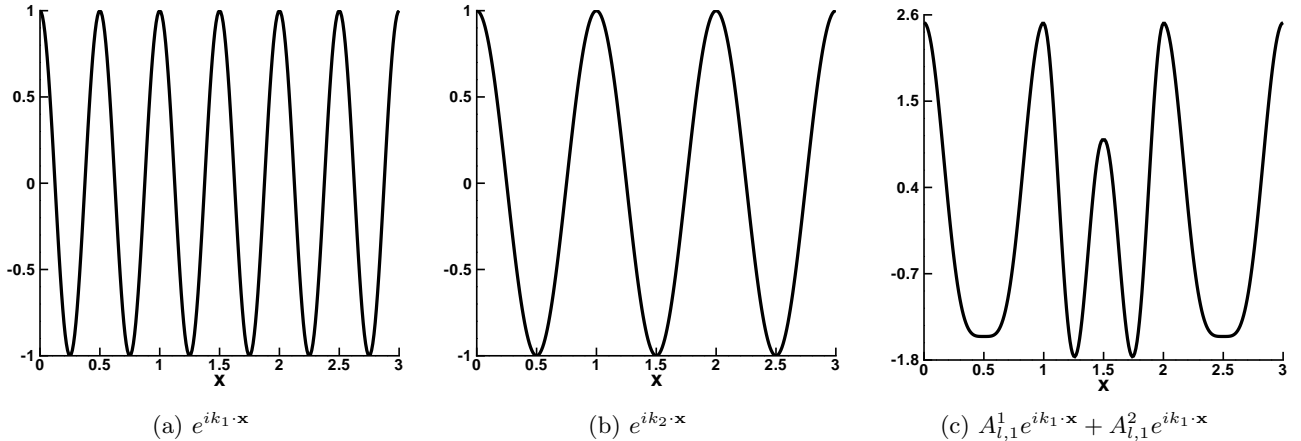


Figure 2: Illustration of plane waves with two different wavenumbers k_1 and k_2 , and a linear combination of the two plane waves used for scattering waves.

3.1 Wave scattering

We consider a computational domain composed of two media such that the wavenumber is constant within each medium but changes suddenly on the interfaces in between these media. To enrich the solution space we use plane waves which were proved to be very successful for this type of problems [12, 19]. Here two sets of plane waves are used each of a different wavenumber. To blend these two sets together the plane waves are applied globally over the entire domain. It should be noted that with the FEM there is no need to consider interface conditions because the boundary integral contributions from either sides of the interface cancel each other. However, if the problem is solved with enriching the FEM space with plane waves of different wavenumbers on each side of the interface, a constraint equation needs to be provided in order to ensure the continuity. For example, the continuity across the interface is enforced in [13] using the Lagrange multipliers. Applying constraints may become computationally demanding particularly when multiple discontinuities are accounted. In the current work the plane wave basis of each wavenumber are continuous across the interfaces, hence, no need for Lagrange multipliers.

The nodal value of the pressure at a node l is expressed in terms of the plane waves combination

$$\phi_l = \sum_{q_1=1}^{Q_1} A_{l,q_1}^1 e^{ik_1 \mathbf{d}_{q_1} \cdot \mathbf{x}} + \sum_{q_2=1}^{Q_2} A_{l,q_2}^2 e^{ik_2 \mathbf{d}_{q_2} \cdot \mathbf{x}}, \quad (9)$$

where A_{l,q_1}^1 is the amplitude associated with the q_1 th plane wave of the wavenumber k_1 . Similarly, A_{l,q_2}^2 is the amplitudes associated with the q_2 th plane wave of the wavenumber k_2 . The plane waves are defined using the position vector \mathbf{x} and the direction vector \mathbf{d} . The values of A_{l,q_1}^1 and A_{l,q_2}^2 are then used to build a combination of these plane waves. As a simple illustration Figure 2 shows a possible combination of plane waves in one-dimension. Here the finite element method is used to approximate the values of the unknowns A_{l,q_1}^1 and A_{l,q_2}^2 in order to estimate the best approximation that is built from the enrichment plane waves. Notice that comparing this approach to the domain-based enrichment approaches a combination of plane waves such as the one shown in Figure 2 is not possible. Instead only one type of enrichment can be used in each subdomain.

Using the nodal values (9) to rewrite the approximation (8) we obtain

$$\phi_h = \sum_{l=1}^{N_d} \psi_l \left(\sum_{q_1=1}^{Q_1} A_{l,q_1}^1 e^{ik_1 \mathbf{d}_{q_1} \cdot \mathbf{x}} + \sum_{q_2=1}^{Q_2} A_{l,q_2}^2 e^{ik_2 \mathbf{d}_{q_2} \cdot \mathbf{x}} \right), \quad (10)$$

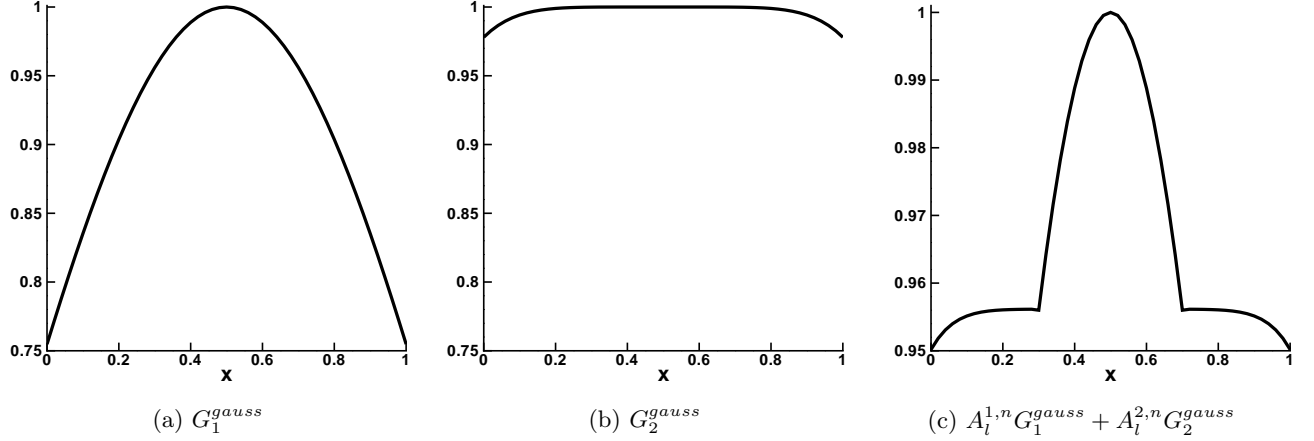


Figure 3: Illustration of two Gaussian functions and a possible linear combination of both functions used for heat transfer.

Thus the approximation space can be rewritten as

$$\tilde{V}_h^1 = \text{span} \left\{ \psi_l e^{ik_1 \mathbf{d}_{q_1} \cdot \mathbf{x}}, \psi_l e^{ik_2 \mathbf{d}_{q_2} \cdot \mathbf{x}}; l = 1, 2, \dots, N_d \text{ with } q_1 = 1, 2, \dots, Q_1 \text{ and } q_2 = 1, 2, \dots, Q_1 \right\}.$$

The enrichment considered in this study can easily be extended to problems of scattering with several heterogeneous media by including a combination of plane wave sets of all the wavenumbers k_1, k_2, k_3, \dots as

$$\phi_h = \sum_{l=1}^{N_d} \psi_l \left(\sum_{q_1=1}^{Q_1} A_{l,q_1}^1 e^{ik_1 \mathbf{d}_{q_1} \cdot \mathbf{x}} + \sum_{q_2=1}^{Q_2} A_{l,q_2}^2 e^{ik_2 \mathbf{d}_{q_2} \cdot \mathbf{x}} + \sum_{q_3=1}^{Q_3} A_{l,q_3}^3 e^{ik_3 \mathbf{d}_{q_3} \cdot \mathbf{x}} + \dots \right). \quad (11)$$

3.2 heat transfer

To enrich the solution space for the two-dimensional heat conduction we use a family of Gaussian functions, as proposed in [26], and defined as

$$G_q^{gauss}(x, y) = \frac{\exp\left(-\left(\frac{R}{C}\right)^{m_q}\right) - \exp\left(-\left(\frac{R_c}{C}\right)^{m_q}\right)}{1 - \exp\left(-\left(\frac{R_c}{C}\right)^{m_q}\right)}, \quad q = 1, 2, \dots, Q, \quad (12)$$

where $R := \|\mathbf{x} - \mathbf{x}_c\|$ is the distance from the function control point $\mathbf{x}_c = (x_c, y_c)^T$ to the point $\mathbf{x} = (x, y)^T$. The control points are located at or close to the lowest gradient of the solution, which is usually at the heat core. The constants R_c and C control the shape and the amplitude of the Gaussian function G_q^{gauss} . Hence, as in (8) the nodal values can be rewritten at any time $t = t_n$ as

$$T_l^n = \sum_{q=1}^Q A_l^{q,n} G_q^{gauss}. \quad (13)$$

As in the scattering waves, the finite element method is now used to approximate the values of the unknowns $A_l^{q,n}$ in order to find the best combination of the enrichment functions to be used for

approximating the finite element solution. A simple illustration of this type of enrichment functions is displayed in Figure 3. Using the nodal values (13) to rewrite the approximation (8) we obtain

$$T_h^n = \sum_{l=1}^{N_d} \sum_{q=1}^Q A_l^{q,n} \psi_j G_q^{gauss}. \quad (14)$$

Thus, the new approximation space becomes

$$\tilde{V}_h^1 = \text{span} \left\{ \psi_h G_q^{gauss}; \quad l = 1, 2, \dots, N_d \quad \text{and} \quad q = 1, 2, \dots, Q \right\}.$$

Because of the composite nature of the considered media, some parts of the domain will heat up or cool down faster than other parts. The enrichment is designed so that the higher orders will recover the steep parts of the solution in one part of the domain whereas the lower orders will approximate the flat parts of the solution in other regions. The discontinuity in the material properties may lead into sharp heat gradients on the material interface or the domain boundaries. The enrichment with high gradient should account for different spatial distribution of steep gradients in the solution.

Since the enrichment functions are time-independent, the system matrix of the linear system resulting from (6) is also time-independent. A major advantage is then the ability to retain the system matrix assembled at the first time step to be re-used at later time steps without alteration. This is achieved by factorizing the system matrix using an LDL^\top decomposition where \mathbf{L} is a lower and \mathbf{D} is a diagonal matrix [1]. This factorization is only done at the first time step where resolving the system is reduced to forward-, diagonal- and back-substitutions at any time step after updating the right-hand side of the system. This can significantly increase the efficiency when a large number of time steps is needed, compared to updating the matrix and fully solving the system if a time-dependent enrichment is to be used. The advantages of the time-independent enrichment are discussed in further details in [14, 19].

4 Numerical results and applications

In this section, several numerical examples are presented to illustrate the efficiency of the PUFEM with the considered enrichment for solving problems in heterogeneous media. The PUFEM is compared to the standard FEM which is widely used for solving problems of this type. In the examples where no analytical solution is available a very fine finite element mesh is used to recover a reference solution. The efficiency of the PUFEM is demonstrated here by achieving a similar accuracy to the FEM but with a much lower number of degrees of freedom.

4.1 Acoustic wave scattering

Considering the wave scattering in the heterogeneous media depicted in Figure 1 a reference solution can be obtained using the procedure introduced in [13]. Thus, the pressure at a point in the region Ω_1 is given as

$$\phi_1 = \sum_{n=0}^{\infty} \left(A_n J_n(k_1 r) + B_n Y_n(k_1 r) \right) \cos(n\theta), \quad (15)$$

while the pressure for a point in region Ω_2 is

$$\phi_2 = \sum_{n=0}^{\infty} \left(C_n J_n(k_2 r) + D_n Y_n(k_2 r) \right) \cos(n\theta), \quad (16)$$

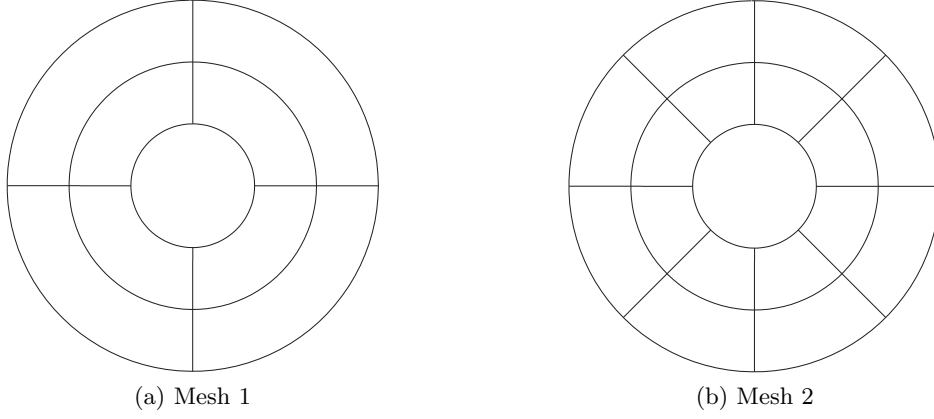


Figure 4: Mesh configurations for wave scattering in a medium with single jump.

where J_n and Y_n are the Bessel functions of order n and of the first and the second kind, respectively. The coefficients A_n, B_n, C_n and D_n can be determined using the boundary conditions. The sound hard implies

$$\mathbf{n}(\hat{\mathbf{x}}) \cdot \nabla \phi_1 = 0, \quad \text{on} \quad \Gamma_s. \quad (17)$$

Continuity of the acoustic pressure gives

$$\phi_1 = \phi_2, \quad \text{on} \quad \Gamma_{int}. \quad (18)$$

The continuity of the normal component of a particle velocity on the interface gives

$$\frac{1}{\rho_1} \mathbf{n}(\hat{\mathbf{x}}) \cdot \nabla \phi_1 = \frac{1}{\rho_2} \mathbf{n}(\hat{\mathbf{x}}) \cdot \nabla \phi_2, \quad \text{on} \quad \Gamma_{int}. \quad (19)$$

Recall that the approximate condition for ϕ_2 on Γ_r in (2) is given by

$$\mathbf{n}(\hat{\mathbf{x}}) \cdot \nabla \phi_2 = \mathbf{n}(\hat{\mathbf{x}}) \cdot \nabla \phi_2^{\text{inc}} + \left(\frac{1}{2r_3} - ik_2 \right) \phi_2^{\text{inc}} - \left(\frac{1}{2r_3} - ik_2 \right) \phi_2, \quad (20)$$

where the incident wave ϕ_2^{inc} can be expanded using the following series

$$\phi_2^{\text{inc}} = J_0(k_2 r) + \sum_{n=1}^{\infty} 2i^n J_n(k_2 r) \cos(n\theta). \quad (21)$$

It is evident that the equations (17)-(21) can be used to evaluate the coefficients A_n, B_n, C_n , and D_n for a given number of terms in the series expansion. Once these coefficients are known, the total pressure can be computed at any point in Ω using (15) and (16).

4.1.1 Plane wave scattering in a medium with single jump.

We consider plane wave scattering in a medium with a jump in the density (and hence in the wavenumber) using the configuration shown in Figure 1. Here the various radii for the geometry are $r_1 = 1$, $r_2 = 2$ and $r_3 = 3$. For numerical integration inside a given finite element the standard Gaussian quadrature is used. It should be pointed out that for the PUFEM we use n_g integration points per wavelength in each dimension. For the results presented in this section $n_g = 10$, which is a common practice when solving wave problems [12]. In all our simulations, the integration points are placed analytically on the geometry. To give an overall estimate of the problem size we define a parameter $nDof$ which is the total number of degrees of freedom. This number is equal to the total

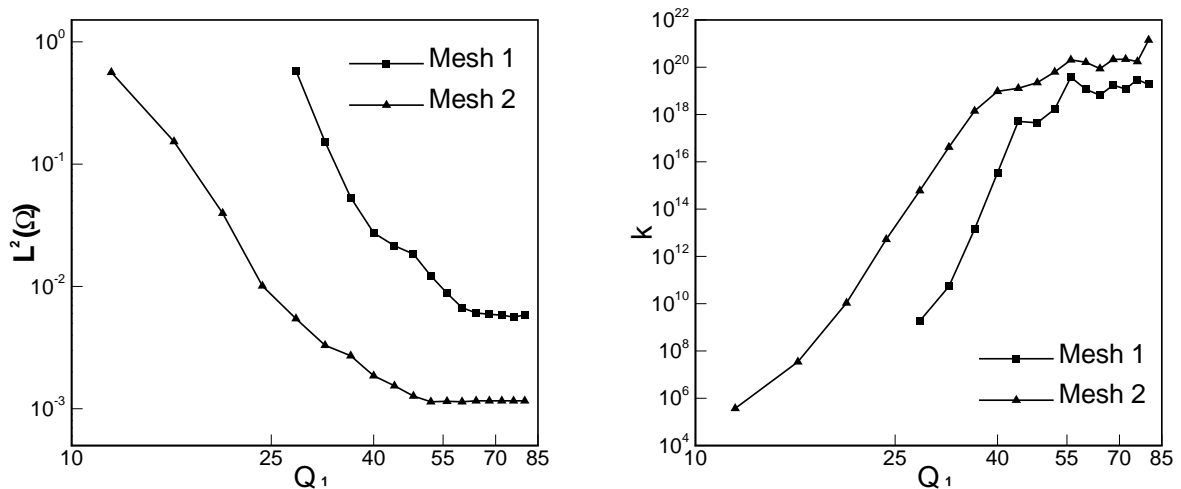


Figure 5: Evolution of the relative error $L^2(\Omega)$ (left plot) and the condition number (right plot) with increasing the number of plane waves where $Q_1 = Q_2$.

number of nodes in the conventional FEM while it is equal to the total number of nodes multiplied by the total number of enrichment functions in the PUFEM. We also define the relative L^2 error by

$$L^2(\Omega) = \frac{\left(\int (\phi - \tilde{\phi})^2 d\Omega \right)^{\frac{1}{2}}}{\left(\int \phi^2 d\Omega \right)^{\frac{1}{2}}}, \quad (22)$$

where ϕ is the reference solution calculated using (17)-(21) and $\tilde{\phi}$ is the numerical solution. Similarly, the relative $L^2(\Gamma_s)$ error on the scatterer can be computed using the relevant line integrals on the scatterer boundary.

First, we examine the q -refinement in the PUFEM using the considered meshes shown in Figure 4 where we refer to the coarse and the fine meshes as Mesh 1 and Mesh 2, respectively. In this test example we use a uniform choice of the numbers of the enrichment functions *i.e.* the number of plane waves used for enrichment with wavenumbers k_1 and k_2 are equal ($Q_1 = Q_2$). We summarize in Figure 5 the relative errors $L^2(\Omega)$, and the condition number $\log_{10}(k)$ obtained with increasing the numbers of enrichment. As expected smaller errors are obtained on the fine mesh than the coarse mesh. Increasing the number of enriching plane waves reduces the error exponentially. The large values of the condition number should also be noted which is often observed with the PUFEM [12]. It is worth adding that solving the wave scattering problem discussed here with the conventional FEM is very demanding. For example, solving the same problem using the FEM on linear triangular elements with 117568 degrees of freedom, results in an $L^2(\Omega)$ -error of 12%, which despite this relatively high number of degrees of freedom is at least one order of magnitude larger than any of the PUFEM results presented here.

In Figure 6 we present the PUFEM results obtained on Mesh 2 using $k_1 = 2\pi$ and $k_2 = 4\pi$, where the real and imaginary parts of the total pressure are plotted against the reference solution. As can be seen from the displayed results, there is no visual difference between the PUFEM solution and the reference solution. The PUFEM accurately resolves this test problem on a reasonably coarse mesh and without any special treatment of the interface between the two media such as Lagrange multipliers discussed in [13, 8] for acoustics and in [6] for electromagnetics.

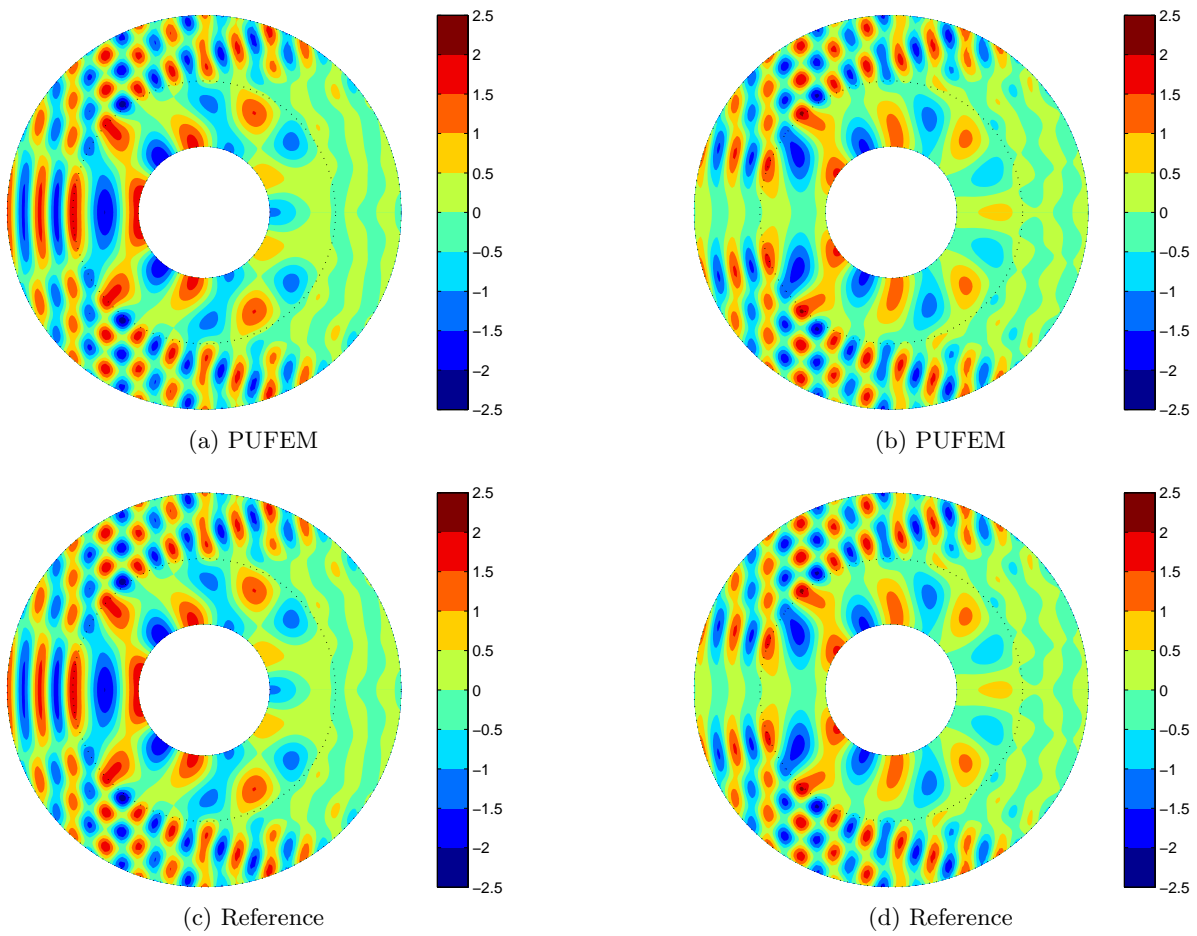


Figure 6: Real part (first column) and imaginary part (second column) of total pressure for wave scattering in a medium with single jump using $k_1 = 2\pi$ and $k_2 = 2k_1$.

Table 1: Results for q -refinement in the PUFEM for wave scattering in a medium with single jump using Mesh 2 and for $k_1 = 2\pi$ and $k_2 = 8\pi$ or 12π .

k_2/k_1	Case	Q_1	Q_2	$nDof$	$L^2(\Gamma_s)$	$L^2(\Omega)$	$\log_{10}(\kappa)$
4	1	2	12	336	5.56E-02	4.18E-02	4.55
	2	4	12	384	1.75E-02	1.65E-02	6.7
	3	6	12	432	1.21E-02	1.17E-02	8.23
	4	8	12	480	8.70E-03	8.94E-03	10.16
6	5	8	24	768	3.57E-02	2.11E-02	10.08
	6	12	24	864	2.47E-02	1.45E-02	13.37
	7	16	24	960	1.02E-02	5.99E-03	16.79
	8	20	24	1056	9.37E-03	5.45E-03	18.74

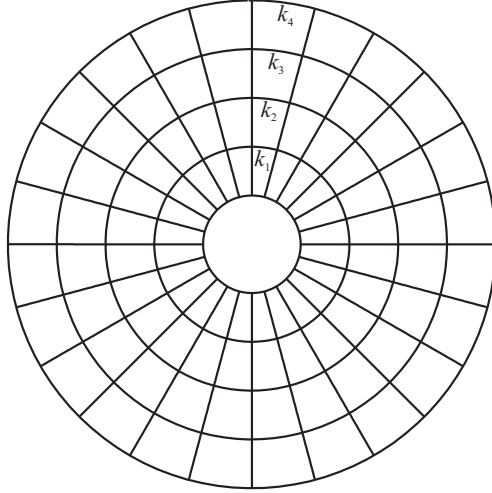


Figure 7: Mesh used for the wave scattering in a medium with multiple jumps.

Our next concern is to study the effect of changing one of the enrichment numbers Q_1 while keeping the other number Q_2 constant. The magnitude of the jump is taken into account by considering two ratios of k_2/k_1 . Here we refer to increasing the total number of enrichment functions as the q -refinement. In Table 1 we list the PUFEM results on Mesh 2 for the wavenumbers $k_1 = 2\pi$ and $k_2 = 8\pi$ or 12π . It is evident that the PUFEM can predict accurate solutions even for higher values of the ratio k_2/k_1 . Furthermore, the PUFEM can clearly work with an unequal choice of enrichment numbers. Indeed this choice can significantly reduce the condition number by almost six orders of magnitude for $k_2/k_1 = 4$ and eight orders of magnitude for $k_2/k_1 = 6$ while only increasing the L^2 -error by one order of magnitude. It should also be stressed that to solve the linear systems resulted from the PUFEM we used the Singular Value Decomposition (SVD) algorithm [9]. The performance of the SVD solver for solving highly ill-conditioned systems as those obtained in the current study is commonly well-established, compare for example [10].

4.1.2 Plane wave scattering in a medium with multiple jumps.

Next we solve the problem of wave scattering in a medium with multiple jumps in the density. We consider a sound hard cylinder surrounded by four concentric fluid layers as shown in Figure 7 with

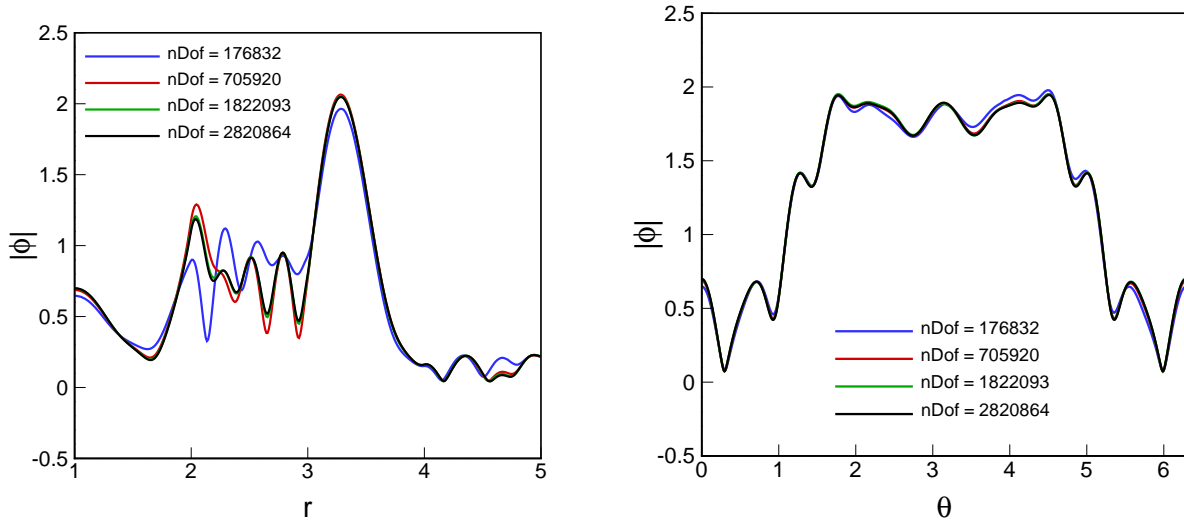


Figure 8: Cross sections of the modulus $|\phi|$ at $\theta = 0$ (left plot) and on Γ_s (right plot) using $k_1 = k_3 = 2\pi$ and $k_2 = k_4 = 2k_1$.

wavenumbers $k_1 = k_3$ and $k_2 = k_4$. As in the previous example, we use linear quadrilateral finite elements for the spatial discretization, see Figure 7. The FEM result on a fine mesh is used as a reference solution. Although in theory it is possible to obtain a reference solution following the approach (17)-(21), but in practice the resulting linear system of equations for the reference solution can become a singular system leading to unstable results. It is for this reason, only reference results obtained using the FEM are included for the comparison.

First, we examine the h -convergence of the FEM for this test example. To this end the problem is solved on a relatively coarse mesh with $nDof = 176832$ using $k_1 = k_3 = 2\pi$ and $k_2 = k_4 = 2k_1$. Then the problem is solved on three finer meshes for each subsequent solution. The value of $nDof$ is hence increased to 705920, 1822093 and 2820864. Figure 8 shows two cross sections of the total pressure $|\phi|$ at $\theta = 0$ and on Γ_s for the four different solutions. It is clear that the FEM converges as the characteristic size of each element in the mesh is reduced. The FEM solution with $nDof = 1822093$ is practically identical to that with $nDof = 2820864$ which is taken as a reference solution. To further compare the PUFEM to the standard FEM we present in Figure 9 the PUFEM results on the same cross sections as above against the FEM reference solution. It is clear that the PUFEM with $nDof = 5760$ accurately capture the same solution as the FEM on the finest mesh. It should be stressed that the FEM with $nDof = 705920$ could not achieve the same accuracy as the PUFEM. The former result shows some differences when compared to the converged solution. Thus the significant saving in the total number of degrees of freedom (more than 99%) with the PUFEM is evident. For comparison purpose we have also included in Figure 10 two-dimensional plots of the PUFEM results against the reference solution obtained using $k_1 = k_3 = 2\pi$ and $k_2 = k_4 = 2k_1$ whereas, those obtained using $k_1 = k_3 = \pi/2$ and $k_2 = k_4 = 4k_1$ are presented in Figure 11. It is clear that the PUFEM accurately capture the small wave features in this problem and produces similar scattering patterns as those of the reference solution.

4.2 Transient heat transfer

To ascertain the performance of the PUFEM we consider two test examples of heat conduction in a composite with inclusions. In the first example we solve the problem of heat conduction in a

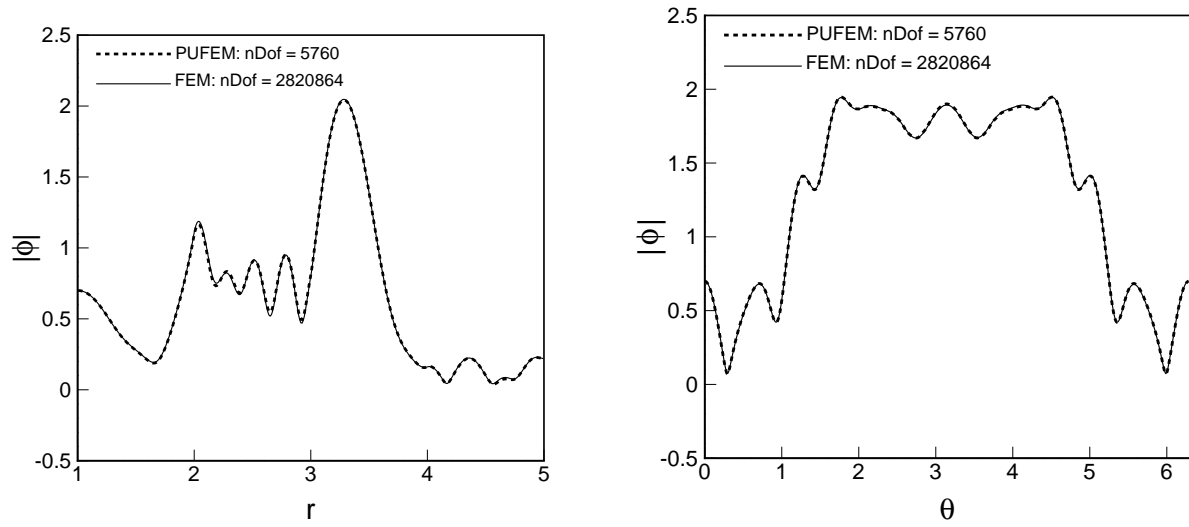


Figure 9: Cross sections of the modulus $|\phi|$ at $\theta = 0$ (left plot) and on Γ_s (right plot) using $k_1 = k_3 = 2\pi$ and $k_2 = k_4 = 2k_1$.

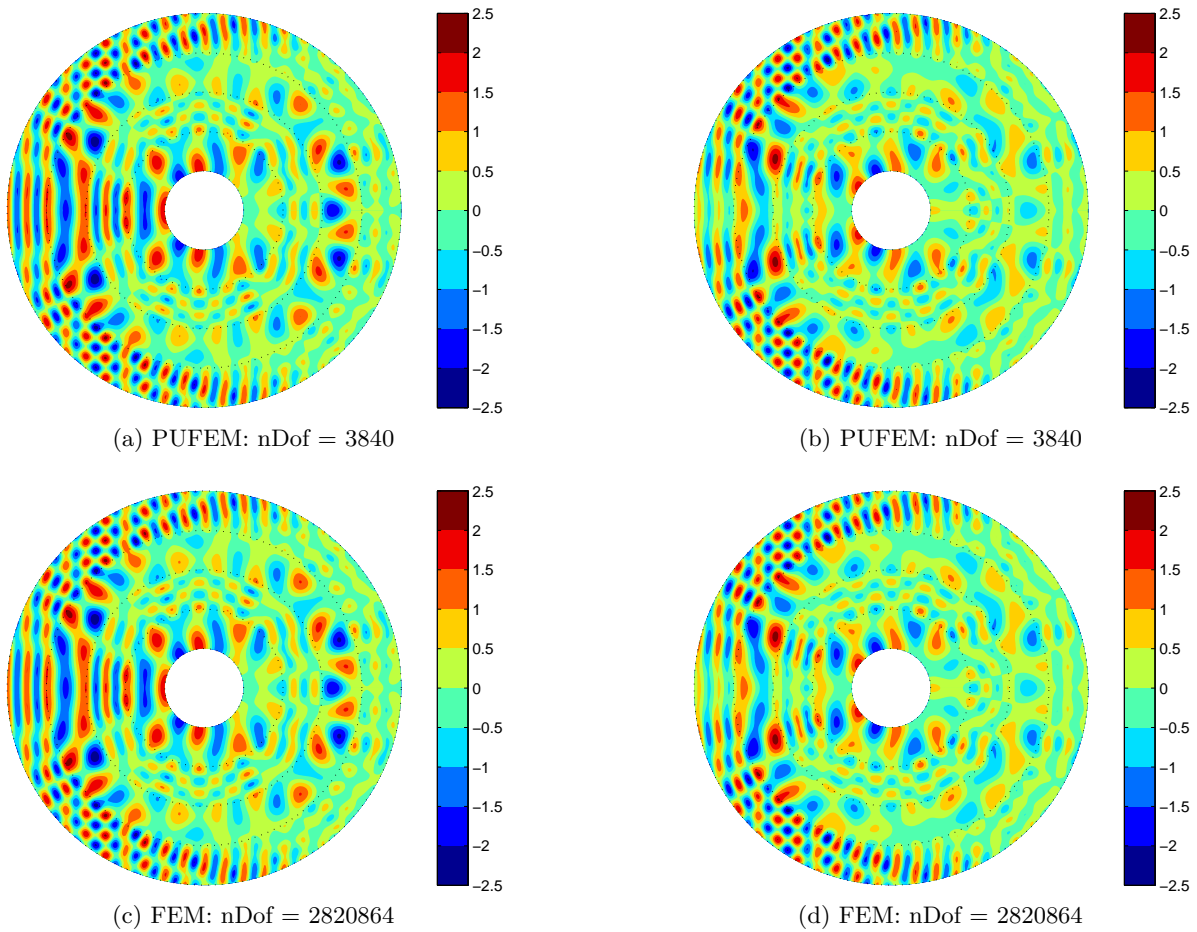
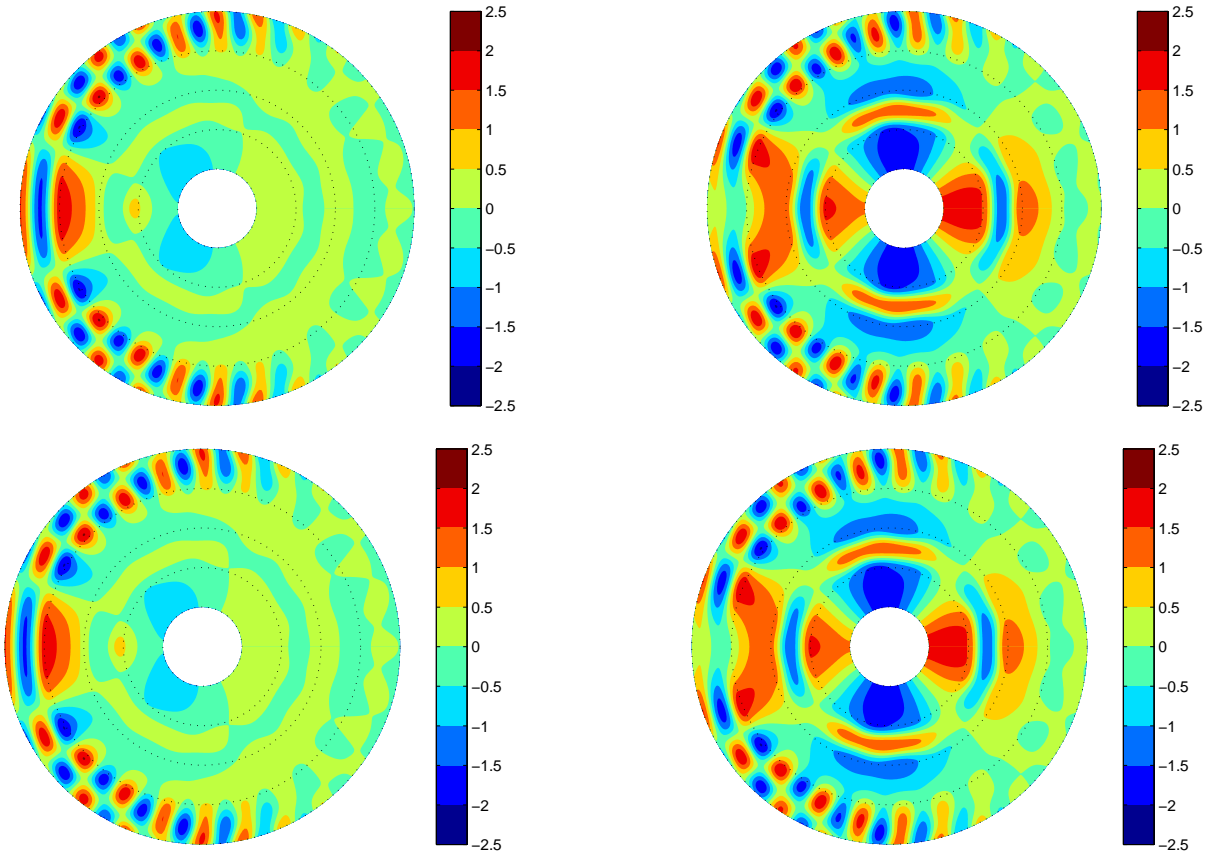


Figure 10: Real part (first column) and imaginary part (second column) of total pressure for wave scattering in a medium with multiple jumps using $k_1 = k_3 = 2\pi$ and $k_2 = k_4 = 2k_1$.



(c) FEM: nDof = 2820864

(d) FEM: nDof = 2820864

Figure 11: Real part (first column) and imaginary part (second column) of total pressure for wave scattering in a medium with multiple jumps using $k_1 = k_3 = \pi/2$ and $k_2 = k_4 = 4k_1$.

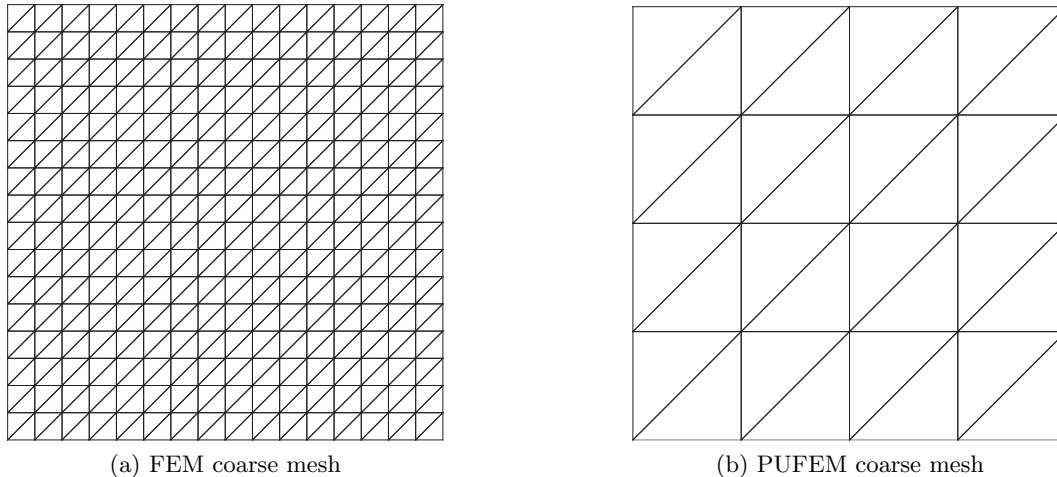


Figure 12: Structured FEM coarse mesh (left plot) and PUFEM coarse mesh (right plot) for the test example of heat conduction in a composite with single inclusion.

composite with a single inclusion and subject to a heated boundary from the surrounding medium. A moving thermal front from the boundary towards the center of the composite is expected in this example. The form and speed of the thermal front depend on the values of conduction coefficients of the inclusion. In the second test example instantaneous heat sources are accounted for in the problem of heat conduction in a composite with double inclusions. As a consequence, this heat conduction problem is more difficult to handle; the results shown here illustrate the robustness of the PUFEM.

The numerical performance of the PUFEM algorithm described is investigated and numerically verified to show its capability in solving transient heat conduction problems involving nonhomogeneous thermal coefficients. For the purpose of this study a uniform time step is used for the entire time window considered. Unless otherwise mentioned, the time step size Δt is fixed to 10^{-2} with $\theta = \frac{1}{2}$. To evaluate elementary matrix entries all the integrals are evaluated numerically using standard Gaussian quadrature. The number of integration points is chosen to be sufficient so that the results are not affected by the integration errors. In this way it is clear that we are testing the algorithm independently of integration accuracy. We also refer to [26] for detailed discussions on the use of numerical integration with the PUFEM in this type of problems. It should be stressed that for the test examples considered in this paper, the total number of integration points used in the PUFEM is smaller than in the corresponding FEM model. This is true despite the high number of integration points per elements with the PUFEM because of the much lower number of elements in the considered meshes compared to the FEM. The resulting linear systems of algebraic equations are solved using a direct solver.

4.2.1 Heat conduction in a composite with single inclusion.

To investigate the performance of the PUFEM algorithm we consider a linear heat equation with discontinuous conductivity coefficients. The governing equations are of the form (3a)-(3b) with $\rho c = \bar{h} = 1$. Initial temperature $T_0 = 300$, boundary temperature $T_b = 1300$ and the source term $S = 0$. The computational domain is the unit square $\Omega = [0, 1] \times [0, 1]$ while the thermal conductivity is defined by

$$\kappa(\mathbf{x}) = \begin{cases} \kappa_1, & \text{if } \mathbf{x} \in [0.25, 0.25] \times [0.75, 0.75], \\ \kappa_2, & \text{elsewhere.} \end{cases}$$

We consider two heat transfer regimes corresponding to $(\kappa_1 = 10, \kappa_2 = 1)$ and $(\kappa_1 = 1, \kappa_2 = 10)$. All quantities are given with their respective units which are omitted here for simplicity. In order to quantify the errors in this example a reference solution computed using the FEM on a fine mesh of 50625 nodes is used. We consider the relative L^∞ -norm error function $\mathcal{E}_\infty(t_n)$ at time t_n as

$$\mathcal{E}_\infty(t_n) = \frac{\|\bar{T}^n - T^n\|_{L^\infty(\Omega)}}{\|\bar{T}^n\|_{L^\infty(\Omega)}}, \quad (23)$$

where $\|\cdot\|_{L^\infty(\Omega)}$ is the L^∞ norm, T^n and \bar{T}^n are respectively, the computed and reference solutions at time t_n . The reference solution is given by the FEM where the finite element mesh is refined until the h -convergence is achieved. Note that the L^∞ -norm is used to quantify the errors rather than the L^2 -norm as it is crucial to recover the temperature field accurately everywhere in the computational domain in order to have an accurate prediction of the physical properties. The aim of this test example is to compare the results obtained using the proposed PUFEM to those obtained using the standard FEM using different meshes and numbers of enrichment functions. For comparison reasons several structured meshes are obtained by h -refining the coarse meshes illustrated in Figure 12. These coarse meshes (for PUFEM and FEM) are used to compare the PUFEM results against the FEM. Only linear three-noded elements are considered in this test example.

Figure 13 presents the temperature distributions obtained using the PUFEM against the reference solution at the times $t = 0.01$ and 0.4 using $(\kappa_1 = 10, \kappa_2 = 1)$. Those results obtained for the test example with $(\kappa_1 = 1, \kappa_2 = 10)$ are displayed in Figure 14. In both cases the heat is propagating from the hot boundaries to the center of the enclosure at different rates. A faster increase in the interior temperature is detected for the case with $(\kappa_1 = 1, \kappa_2 = 10)$ than the simulations with $(\kappa_1 = 10, \kappa_2 = 1)$. For both methods, the recovered temperature field shows the simulated moving fronts from the boundary walls towards the center of the enclosure. The temperature gradient in the composite material with $(\kappa_1 = 10, \kappa_2 = 1)$ is more sharp than the one obtained for the case with $(\kappa_1 = 1, \kappa_2 = 10)$. Under the considered thermal conditions, the reference FEM and PUFEM produce similar results. To further emphasize this behavior we present in Figure 15 cross sections of the temperature distribution along the main diagonal of the enclosure obtained using the PUFEM and the reference FEM solution for both test cases. As can be seen, the results obtained with the PUFEM show the same temperature features as those obtained using the FEM. It is clear that for the considered thermal conditions in this composite material, both the FEM and the PUFEM resolve the solution dynamics and accurately capture the moving temperature fronts. However, the FEM results are obtained on a fine mesh with 12800 elements and 6561 nodes while, the PUFEM results are computed using a coarse mesh with 512 elements and 289 nodes and 4 enrichment functions, thus offering more than 80% reduction in the total number of degrees of freedom.

To quantify the results obtained using the PUFEM we summarize in Table 2 the L^∞ -error in the temperature obtained using the PUFEM and the reference FEM solution at three instants, $t = 0.01, 0.1$ and 0.4 . We present results for different numbers of enrichments Q and different mesh sizes h . The logarithms of the associated condition numbers $\log_{10}(k)$ are also included in this table. It is evident that, for the two considered conduction cases $(\kappa_1 = 10, \kappa_2 = 1)$ and $(\kappa_1 = 1, \kappa_2 = 10)$, decreasing the mesh size h or increasing the number of enrichments Q results in a decrease in the L^∞ errors. In general a faster decay in the L^∞ errors is observed for the case with $(\kappa_1 = 10, \kappa_2 = 1)$ than the case with $(\kappa_1 = 1, \kappa_2 = 10)$. Note that as time evolves the errors decrease in all the simulation cases. This can be attributed to the fact that larger errors in the temperature are localized at the enclosure walls and the inclusion interfaces where the temperature gradient is very large. Due to the diffusion nature of the problem, smooth solutions are expected as time evolves and small errors in the temperature are obtained. As the steady-state regime develops, the temperature field is expected to be constant in the computational domain and consequently the PUFEM and the reference solutions are expected to produce similar errors in the temperature

Table 2: L^∞ -norm error in the PUFEM obtained for different h -refinement and for an increased enrichment for the test example of heat conduction in a composite with single inclusion with $(\kappa_1 = 10, \kappa_2 = 1)$ and $(\kappa_1 = 1, \kappa_2 = 10)$ at different times. Here $4h_f = 0.25$ corresponding to the coarse PUFEM mesh shown in Figure 12 and Q is the number of enrichments in (14).

Q	h	$(\kappa_1 = 10, \kappa_2 = 1)$				$(\kappa_1 = 1, \kappa_2 = 10)$			
		$\log_{10}(k)$	$t = 0.01$	$t = 0.1$	$t = 0.4$	$\log_{10}(k)$	$t = 0.01$	$t = 0.1$	$t = 0.4$
3	$4h_f$	7.92	0.0138	0.0113	0.0060	6.99	0.0062	0.0103	0.0039
	$2h_f$	9.40	0.0056	0.0035	0.0012	8.41	0.0045	0.0034	0.0015
	h_f	10.90	0.0020	0.0022	0.0006	9.89	0.0017	0.0011	0.0005
4	$4h_f$	11.41	0.0079	0.0058	0.00269	10.28	0.0051	0.0091	0.00329
	$2h_f$	13.57	0.0032	0.0025	0.00072	12.52	0.0032	0.0029	0.00082
	h_f	15.83	0.0009	0.0019	0.00045	14.77	0.0011	0.0007	0.00018
5	$4h_f$	13.39	0.0052	0.0039	0.00108	12.24	0.0041	0.0056	0.00128
	$2h_f$	15.96	0.0018	0.0026	0.00063	14.90	0.0027	0.0020	0.00055
	h_f	18.15	0.0007	0.0016	0.00036	16.89	0.0014	0.0009	0.00018

field. On the other hand, decreasing the mesh size h or increasing the number of enrichments Q results in an increase in the condition number k in the PUFEM. It should be pointed out that the conditioning issue usually attributed to the PUFEM can be seen clearly in the table. However, a direct solver using double precision was found to produce results of suitable accuracy in the linear system computations presented in this paper. Moreover, the use of a direct solver to decompose the linear system is inevitable in the first time step if backward/forward substitutions are to be reused at later time steps. For larger systems than those considered here an iterative solver might become preferable. This would require a full system solution even though the system matrix remains the same throughout the time domain; however, using the solution vector from the previous time step as a first approximation will be effective in improving convergence of the iterative scheme.

4.2.2 Heat conduction in a composite with two inclusions.

Our second example is the problem of heat conduction in a composite formed by two inclusions with different heat conduction properties. The elementary cell of the considered composite is a cross-sectional circle of radius $r = 1$ and it is assumed to be isotropic in the cross-sectional plane. We assume that none of the materials' properties depends on temperature, so the problem is linear and can be described by the equations (3a)-(3b) with ρ , c , κ and \tilde{h} being functions of the spatial location \mathbf{x} only. In the present example we consider the situation depicted in Figure 16 where the computational domain includes a small square subdomain \mathcal{S}_1 of a side length 0.4 and a large square subdomain \mathcal{S}_2 of a side length $\frac{1}{\sqrt{2}}$. The locations of the subdomains are defined through the corners p_1 and p_2 shown in Figure 16. The composite is initially at temperature $T_0 = 300$ and the ambient temperature is fixed at $T_b = 300$. The thermal conductivity is defined by

$$\kappa(\mathbf{x}) = \begin{cases} 1000, & \text{if } \mathbf{x} \in \mathcal{S}_1, \\ 100, & \text{if } \mathbf{x} \in \mathcal{S}_2, \\ 0.1, & \text{elsewhere.} \end{cases}$$

For this test example, we also consider an instantaneous heat source given by

$$S(t, \mathbf{x}) = \begin{cases} 1000, & \text{if } \mathbf{x} \in \mathcal{S}_1 & \text{and } t \leq 0.4, \\ 1500, & \text{if } \mathbf{x} \in \mathcal{S}_2 & \text{and } t \leq 0.4, \\ 300, & \text{elsewhere} & \text{and } t \leq 0.4. \end{cases}$$

The purpose of this test heat conduction problem is to demonstrate the ability of the PUFEM to compute accurate solutions on very coarse meshes, and also to explore the effects of different levels of enrichment in time domain. Here we consider two unstructured meshes with quadratic six-noded elements as depicted in Figure 17. The fine FEM mesh, with 24470 elements and 49309 nodes, is used to compute a reference solution for the considered test example, whereas the PUFEM mesh has only 30 elements and 71 nodes. It should be noted that capturing the details of the geometry around the close proximity of the two squared subdomains resulted in a relatively large number of elements/nodes with the PUFEM, which otherwise may require even fewer elements/nodes.

Figure 18 presents the temperature distributions obtained using PUFEM at four different instants $t = 0.4, 0.6, 1$ and 2.4 which correspond to the end of the sources' application and at three intervals thereafter. The corresponding results obtained using the fine FEM mesh are not included in this figure because visually they are indistinguishable from the PUFEM results. To obtain this set of results, an enrichment level $Q = 3$ was used, *i.e.* three Gaussian functions were used to enrich the approximation space. Throughout the simulations, the results obtained using the PUFEM exhibit the same temperature trends as those obtained using the fine FEM reference solution. It is evident that for the considered thermal conditions, the PUFEM captures the heat dynamics and accurately resolves the moving temperature fronts. However, the FEM results are obtained on a fine mesh while, the PUFEM results are computed using a coarse mesh with just 213 degrees of freedom. This represents a significant reduction of the total number of DoFs over the FEM model containing 49309 degrees of freedom. As can be seen from Figure 18, after a temperature increase due to the heat source in the inclusions, the source ceases and the composite material starts to cool down. For both PUFEM and FEM approaches, the temperature field shows the simulated moving fronts from the source location towards the walls at the surrounding temperature.

To have a clearer comparison between the results obtained using the PUFEM and those obtained using FEM, we present in Figure 19 the temperature distributions along the cross sectional axis s on the main diagonal passing through the points p_1 and p_2 , as shown in Figure 16. The results are displayed on the left hand side for the warming phase (corresponding to $t \leq 0.4$) and on the right hand side for the cooling phase (corresponding to $t > 0.4$). For comparison reasons, the results obtained using the FEM on the fine mesh shown in Figure 17 are also included in Figure 19. It is clear that the PUFEM results are capturing the temperature solution well throughout the simulation, including an accurate prediction of the weak discontinuities at the material interfaces.

Finally, in Figures 20 and 21 we plot the time evolution of the temperature at the points p_1 and p_2 respectively, found from the FEM and PUFEM approximations. The effect of the source turning on at $t = 0$ and off at $t = 0.4$ is very clearly seen here, and the PUFEM model using three enrichment functions (labelled "PUFEM3") is matching the FEM results closely. Also in these figures we plot the temperature difference, dT , between the PUFEM and FEM results for a range of PUFEM approximations using 3, 4 and 5 Gaussian enrichment functions (labelled "PUFEM3", "PUFEM4" and "PUFEM5"). The general behavior of all three sets of results is similar, and show that a greater level of enrichment yields greater accuracy. However, it is interesting to note that, at point p_1 , the errors from the PUFEM3 simulation are, unexpectedly, lower than those using four and five enrichment functions during the time interval $0.4 \leq t \leq 2$. This apparent anomaly is resolved upon closer examination of the results. We find that, in general, errors in temperature predictions are manifested in the model heating up and cooling down too slowly. Thus, during the

warming up phase ($0 \leq t \leq 0.4$) the PUFEM5 results are the most accurate, while PUFEM3 and PUFEM4 are predicting a slightly lower temperature than that required. At the start of the cooling down phase ($t \geq 0.4$), then, the PUFEM3 and PUFEM4 simulations are already at a slightly cooler temperature, and are therefore temporarily more capable of finding an accurate solution in these time steps. After further time steps, normal behavior is resumed and the higher level of enrichment results in the lower errors.

5 Conclusions

The partition of unity finite element method is extended into a heterogeneous media by blending the enrichment functions of each material/subdomain into a global enrichment which is then applied over the entire domain. The enrichment continuity is naturally ensured without having to enforce it between the subdomains as in previous approaches. On the other hand the weak discontinuities of the materials interface are approximated by the finite elements polynomial shape functions. The extension has a wide range of applications especially in problems of multiple scales of interest. Applications to wave scattering and to transient heat transfer are presented. In each application examples of a single and then multiple inclusions of discontinuous physical properties are presented. Numerical comparisons have been carried out for all the considered problems in terms of the solution field and the error convergence.

Two different applications namely wave scattering and heat transfer are considered. For wave scattering the considered examples include a single jump and multiple jumps in the wavenumber where the jump amplitude is heightened. The studied enrichment combines plane waves of two different wavenumbers. To solve the examples first for each wavenumber the same number of plane waves is used. Then the number of enriching plane waves corresponding to the lowest wavenumber, is decreased while the number of plane waves corresponding to the higher wavenumber, is fixed. This helped to improve the condition number by eight orders of magnitude while only changing the error by one order of magnitude. The approach dealt satisfactorily with multiple jumps. It leads to a significant reduction in the total number of degrees of freedom compared to the FEM in order to achieve a given accuracy. For the heat transfer applications two numerical examples are presented. Heat conduction with discontinuous thermal properties are studied in composites of two and three different materials. Exponential functions of different gradients are combined to enrich the solution space. The obtained results show good heat resolution and lower numerical dissipation. The PUFEM captures the steep gradients in the temperature field without nonphysical oscillations and excessive numerical diffusion even when coarse meshes and large time steps are used in the computations.

The efficiency of the method comes from the coarse nature of the meshes used in the spatial discretization. It should be noted as well that the symmetry of the linear system is preserved and a profile solver can be used for a fast solution. Furthermore and in the time domain this class of enrichment functions produces a time-independent matrix representation of the problem that gives very important gains in computational efficiency since it is only at the first time step that the matrix needs to be reduced. In all the considered examples, we have observed that for a fixed accuracy the total number of degrees of freedom may be reduced by up to 95% when the PUFEM is used which makes it an attractive alternative to problems in heterogeneous media compared to the standard finite element method. Future work will concentrate on developing efficient solvers for the associated linear systems in order to deal with the conditioning issue and developing efficient analytical integration schemes. Extension of the presented techniques to three space dimensions is of particular interest as it will result in an extensive save in the computational resources compared to the conventional finite element methods.

References

- [1] Peter Bettess and Jacqueline A Bettess. A profile matrix solver with built-in constraint facility. *Engineering Computations*, 3(3):209–216, 1986.
- [2] O. Cessenat and B. Despres. Application of the ultra-weak variational formulation of elliptic pde's to the two-dimensional Helmholtz problem. *SIAM J. Numer. Anal.*, 35:255–299, 1998.
- [3] J.D. Chazot, B. Nennig, and E. Perrey-Debain. Performances of the partition of unity finite element method for the analysis of two-dimensional interior sound fields with absorbing materials. *Journal of Sound and Vibration*, 2012.
- [4] J.M. Dlugach, M.I. Mishchenko, L. Liu, and D.W. Mackowski. Numerically exact computer simulations of light scattering by densely packed, random particulate media. *Journal of Quantitative Spectroscopy and Radiative Transfer*, 112(13):2068 – 2078, 2011. *Polarmetric Detection, Characterization, and Remote Sensing*.
- [5] Yaniv Edery, Alberto Guadagnini, Harvey Scher, and Brian Berkowitz. Reactive transport in disordered media: Role of fluctuations in interpretation of laboratory experiments. *Advances in Water Resources*, 2011.
- [6] Werley G. Facco, Elson J. Silva, Ricardo Adriano, Alex S. Moura, and Nasses Z. Lima. Handling material discontinuities in a nonconforming generalized finite element method to solve wave propagation problems. *Microwave and Optical Technology Letters*, 54(12):2709–2716, 2012.
- [7] C. Farhat, I. Harari, and L.P. Franca. The discontinuous enrichment method. *Comput. Methods Appl. Mech. Engrg.*, 190:6455–6479, 2001.
- [8] C. Farhat, I. Harari, and U. Hetmanuk. A discontinuous Galerkin method with Lagrange multipliers for the solution of Helmholtz problems in the midfrequency regime. *Comput. Methods Appl. Mech. Engrg.*, 192:1389–1419, 2003.
- [9] Gene Golub and William Kahan. Calculating the singular values and pseudo-inverse of a matrix. *Journal of the Society for Industrial & Applied Mathematics, Series B: Numerical Analysis*, 2(2):205–224, 1965.
- [10] Gene Golub and William Kahan. Calculating the singular values and pseudo-inverse of a matrix. *Journal of the Society for Industrial & Applied Mathematics, Series B: Numerical Analysis*, 2(2):205–224, 1965.
- [11] T. Huttunen, P. Gamallo, and R.J. Astley. Comparison of two wave element methods for the Helmholtz problem. *Commun. Numer. Meth. En.*, 25:35–52, 2009.
- [12] O. Laghrouche, P. Bettess, and R.J. Astley. Modelling of short wave diffraction problems using approximating systems of plane waves. *Int. J. Numer. Meth. Engng.*, 54:1501–1533, 2002.
- [13] O. Laghrouche, P. Bettess, E. Perrey-Debain, and J. Trevelyan. Wave interpolation finite elements for helmholtz problems with jumps in the wave speed. *Computer methods in applied mechanics and engineering*, 194(2):367–381, 2005.
- [14] O. Laghrouche and M.S. Mohamed. Locally enriched finite elements for the Helmholtz equation in two dimensions. *Comput. Struct.*, 88:1469–1473, 2010.
- [15] S. Langdon and S.N. Chandler-Wilde. A wavenumber independent boundary element method for an acoustic scattering problem. *SIAM J. Numer. Anal.*, 43:2450–2477, 2006.

- [16] J.M. Melenk and I. Babuška. The partition of unity finite element method: Basic theory and applications. *Comput. Methods Appl. Mech. Engrg.*, 139:289–314, 1996.
- [17] M.F. Modest. *Radiative Heat Transfer*. McGraw-Hill, 1993.
- [18] M Shadi Mohamed, Mohammed Seaid, Jon Trevelyan, and Omar Laghrouche. An enriched finite element model with h -refinement for radiative boundary layers in glass cooling. *Journal of Computational Physics*, 2013.
- [19] M.S. Mohamed, A. El-Kacimi, and O. Laghrouche. Some numerical aspects of the PUFEM for efficient solution of 2D Helmholtz problems. *Comput. Struct.*, 88:1484–1491, 2010.
- [20] J Niessner and R Helmig. Multi-scale modeling of three-phase–three-component processes in heterogeneous porous media. *Advances in Water Resources*, 30(11):2309–2325, 2007.
- [21] P. O’Hara, C.A. Duarte, and T. Eason. Generalized finite element analysis of three-dimensional heat transfer problems exhibiting sharp thermal gradients. *Comput. Methods Appl. Mech. Engrg.*, 198:1857–1871, 2009.
- [22] P. O’Hara, C.A. Duarte, and T. Eason. Transient analysis of sharp thermal gradients using coarse finite element meshes. *Comput. Methods Appl. Mech. Engrg.*, 200:812–829, 2011.
- [23] E. Perrey-Debain, J. Trevelyan, and P. Bettess. Wave boundary elements: a theoretical overview presenting applications in scattering of short waves. *Eng. Anal. Bound. Elem.*, 28:131–141, 2004.
- [24] SS Quek and GR Liu. *Finite Element Method: A Practical Course: A Practical Course*. Butterworth-Heinemann, 2003.
- [25] T. Radek, K. Irina, and F. Charbel. The discontinuous enrichment method for medium-frequency helmholtz problems with a spatially variable wavenumber. *Computer Methods in Applied Mechanics and Engineering*, 268:126–140, 2014.
- [26] M Shadi Mohamed, Mohammed Seaid, Jon Trevelyan, and Omar Laghrouche. A partition of unity fem for time-dependent diffusion problems using multiple enrichment functions. *International Journal for Numerical Methods in Engineering*, 93(3):245–265, 2013.
- [27] M Shadi Mohamed, Mohammed Seaid, Jon Trevelyan, and Omar Laghrouche. Time-independent hybrid enrichment for finite element solution of transient conduction-radiation in diffusive grey media. *Journal of Computational Physics*, 2013.
- [28] Peter MA Sloot and Alfons G Hoekstra. Multi-scale modelling in computational biomedicine. *Briefings in bioinformatics*, 11(1):142–152, 2010.
- [29] S. Soghrati, A.M. Aragón, C.A. Duarte, and P.H. Geubelle. An interface-enriched generalized FEM for problems with discontinuous gradient fields. *Int. J. Numer. Meth. Engrng.*, 89:939–1067, 2012.
- [30] T. Strouboulis, I. Babuška, and R. Hidajat. The generalized finite element method for Helmholtz equation: Theory, computation, and open problems. *Comput. Methods Appl. Mech. Engrg.*, 195:4711–4731, 2006.
- [31] T. Strouboulis, R. Hidajat, and I. Babuška. The generalized finite element method for Helmholtz equation part II: Effect of choice of handbook functions, error due to absorbing boundary conditions and its assessment. *Comput. Methods Appl. Mech. Engrg.*, 197:364–380, 2008.

- [32] R. Tezaur, L. Zhang, and C. Farhat. A discontinuous enrichment method for capturing evanescent waves in multiscale fluid and fluid/solid problems. *Comput. Methods Appl. Mech. Engrg.*, 197:1680–1698, 2008.
- [33] Lonny L Thompson. A review of finite-element methods for time-harmonic acoustics. *The Journal of the Acoustical Society of America*, 119:1315, 2006.
- [34] F.P. van der Meer, R. Al-Khoury, , and L.J. Sluys. Time-dependent shape functions for modeling highly transient geothermal systems. *Int. J. Numer. Meth. Engrg.*, 77:240–260, 2009.
- [35] O.V. Vasilyev, D.A. Yuen, and S. Paolucci. Solving PDEs using wavelets. *Computers in Physics*, 11(5):429 – 358, 1997.
- [36] Hua Wu and Zhao-Liang Li. Scale issues in remote sensing: A review on analysis, processing and modeling. *Sensors*, 9(3):1768–1793, 2009.
- [37] T.T. Yu and Z.W. Gong. Numerical simulation of temperature field in heterogeneous material with the xfem. *Archives of Civil and Mechanical Engineering*, 13(2):199 – 208, 2013.

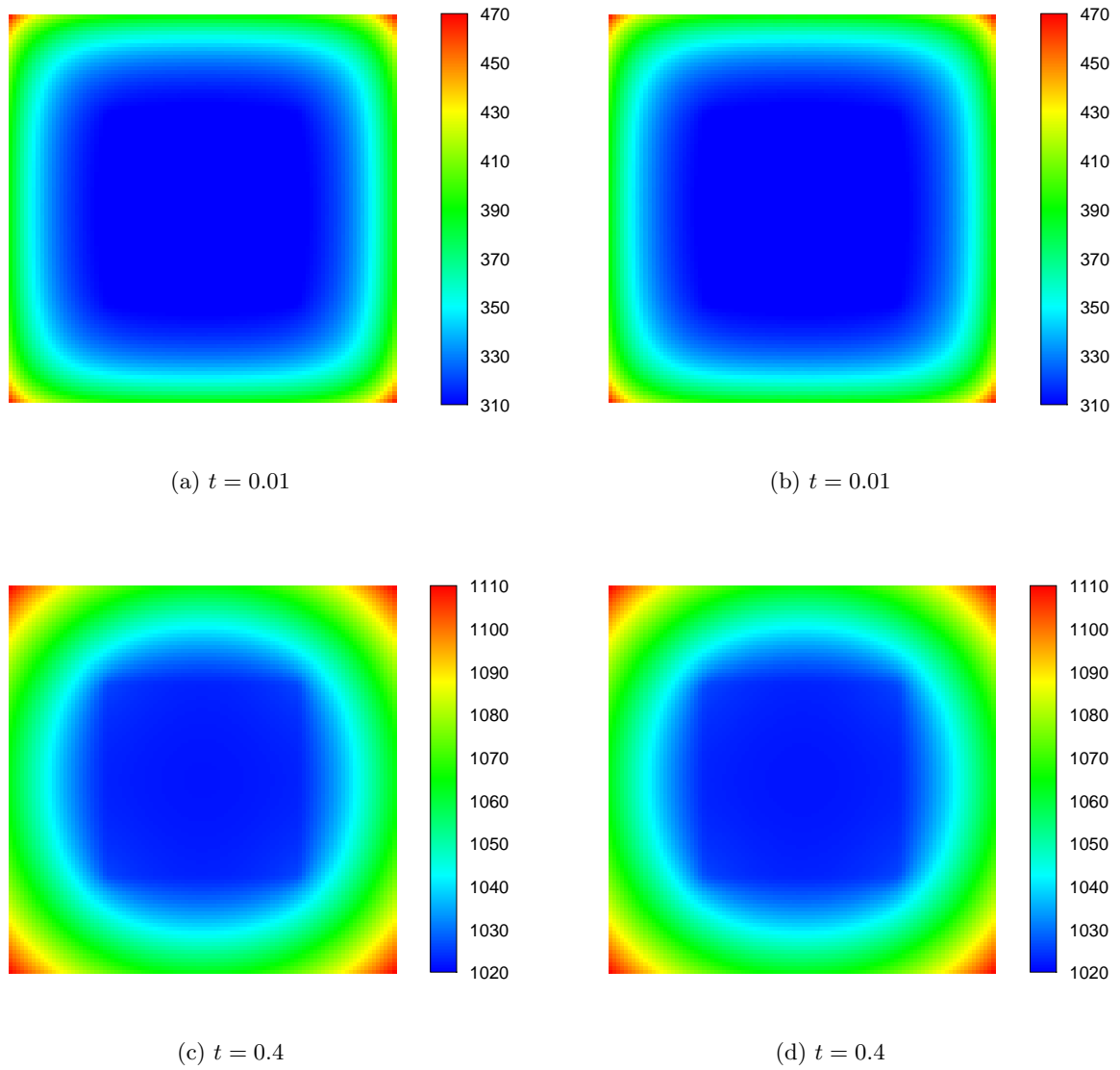
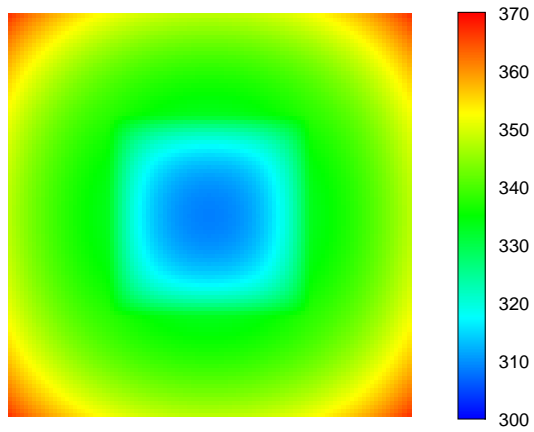
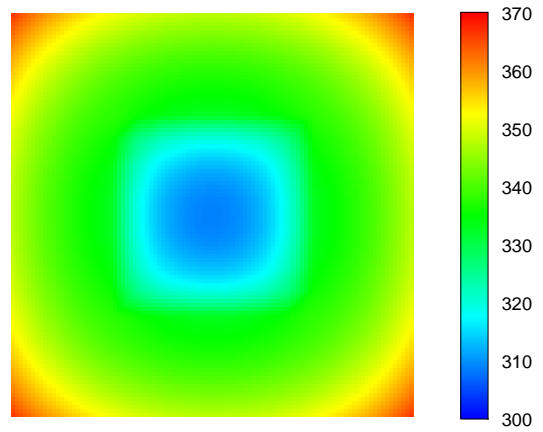


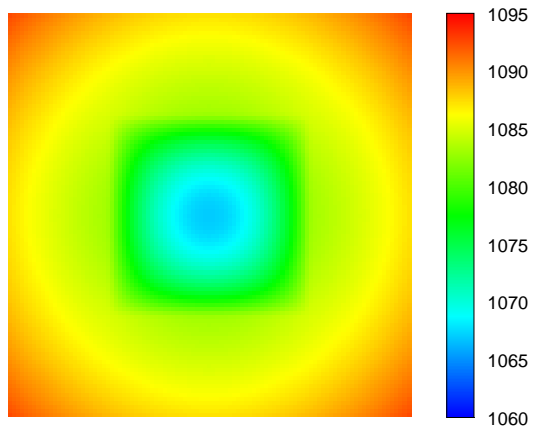
Figure 13: Temperature distributions obtained using the reference FEM (left) and PUFEM (right) for the test example of heat conduction in a composite with single inclusion ($\kappa_1 = 10, \kappa_2 = 1$). Here $t = 0.01$ (first row) and $t = 0.4$ (second row).



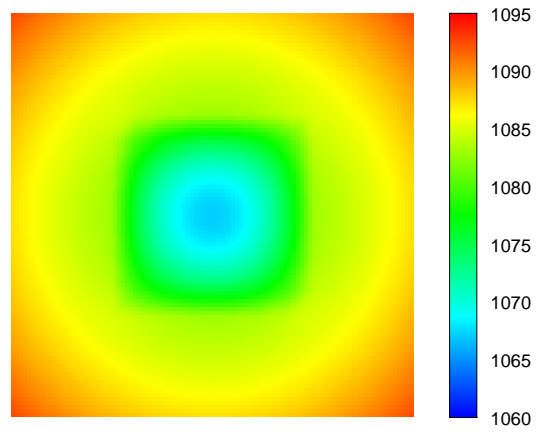
(a) $t = 0.01$



(b) $t = 0.01$



(c) $t = 0.4$



(d) $t = 0.4$

Figure 14: The same as Figure 13 but $(\kappa_1 = 1, \kappa_2 = 10)$.

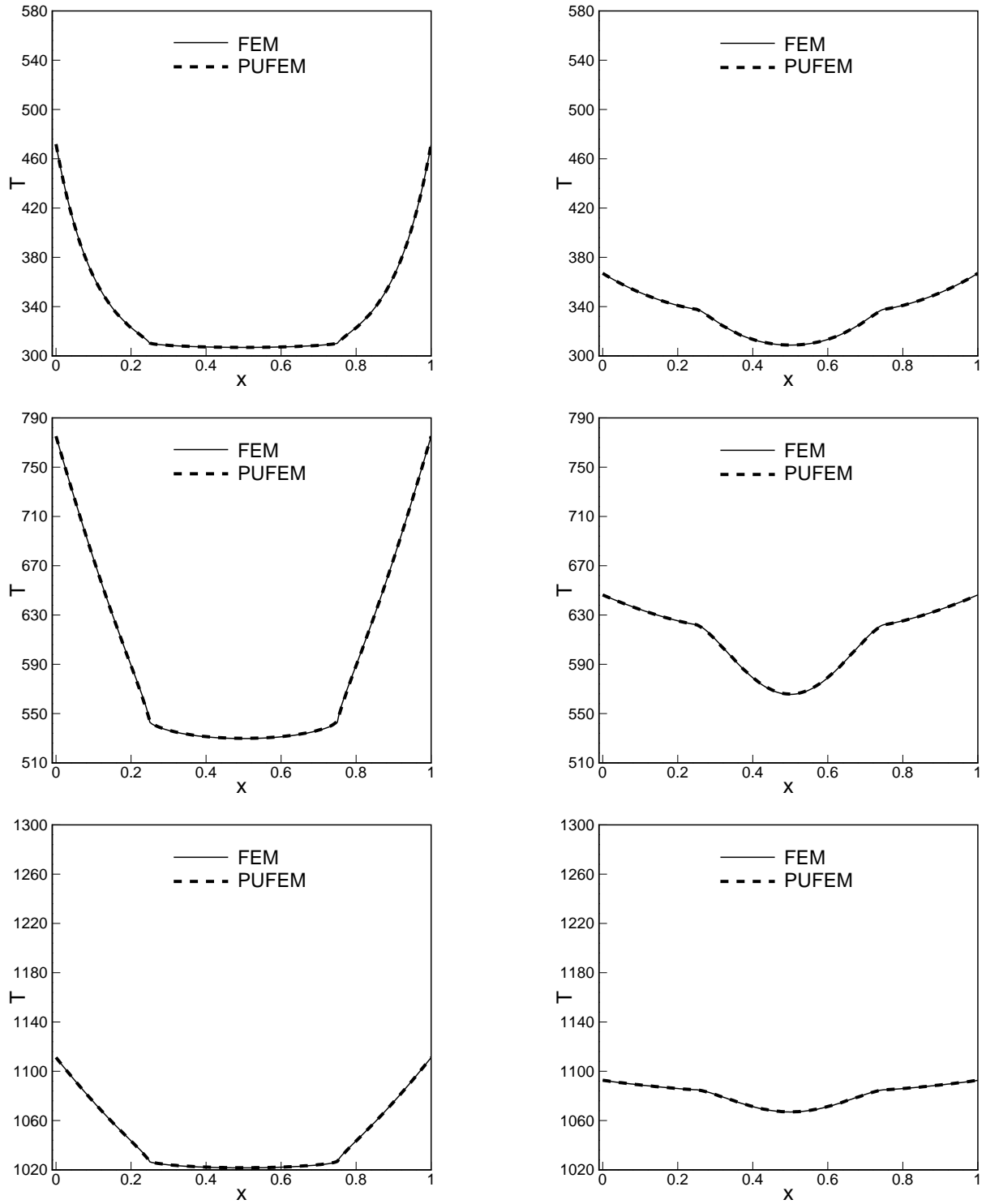


Figure 15: Cross sections of the temperature at the main diagonal at $t = 0.01$ (first row), $t = 0.1$ (second row) and $t = 0.4$ (third row) for the test example of heat conduction in a composite with single inclusion with $(\kappa_1 = 10, \kappa_2 = 1)$ (first column) and $(\kappa_1 = 1, \kappa_2 = 10)$ (second column).

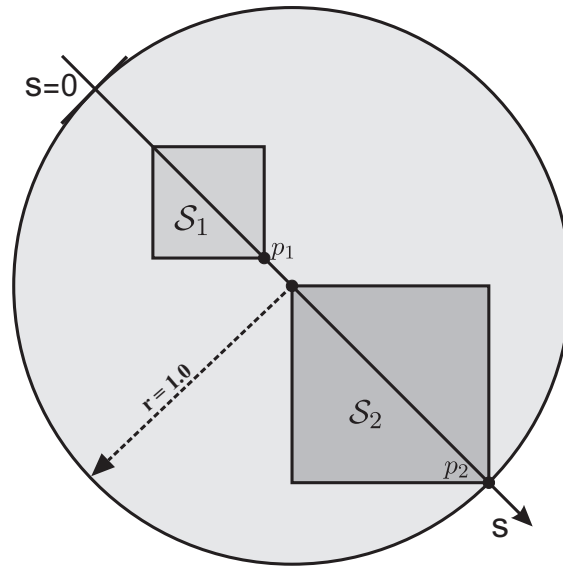
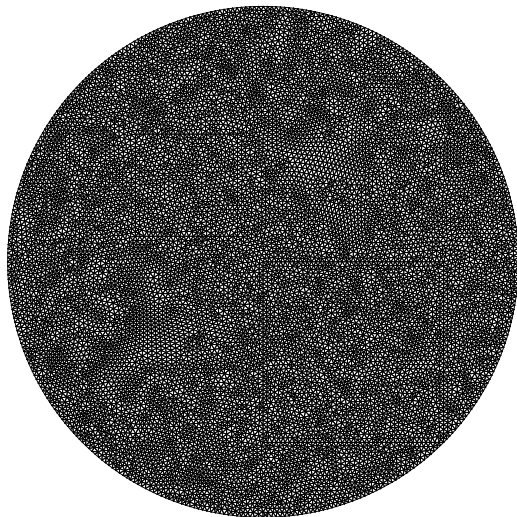
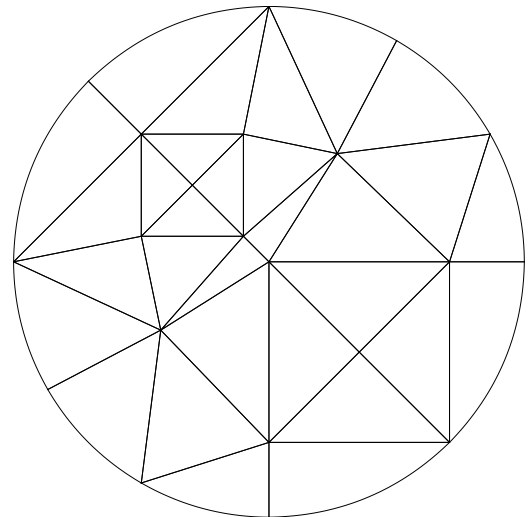


Figure 16: Configuration for the test example of heat conduction in a composite with two inclusions. The axis s lies along the diagonal at 45° to the vertical. The points p_1 and p_2 are located at $s = 1 - 0.1\sqrt{2}$ and $s = 2$, respectively.



(a) FEM: nodes = 49309, elements = 24470.



(b) PUFEM: nodes = 71, elements = 30.

Figure 17: Meshes for the test example of heat conduction in a composite with two inclusions.

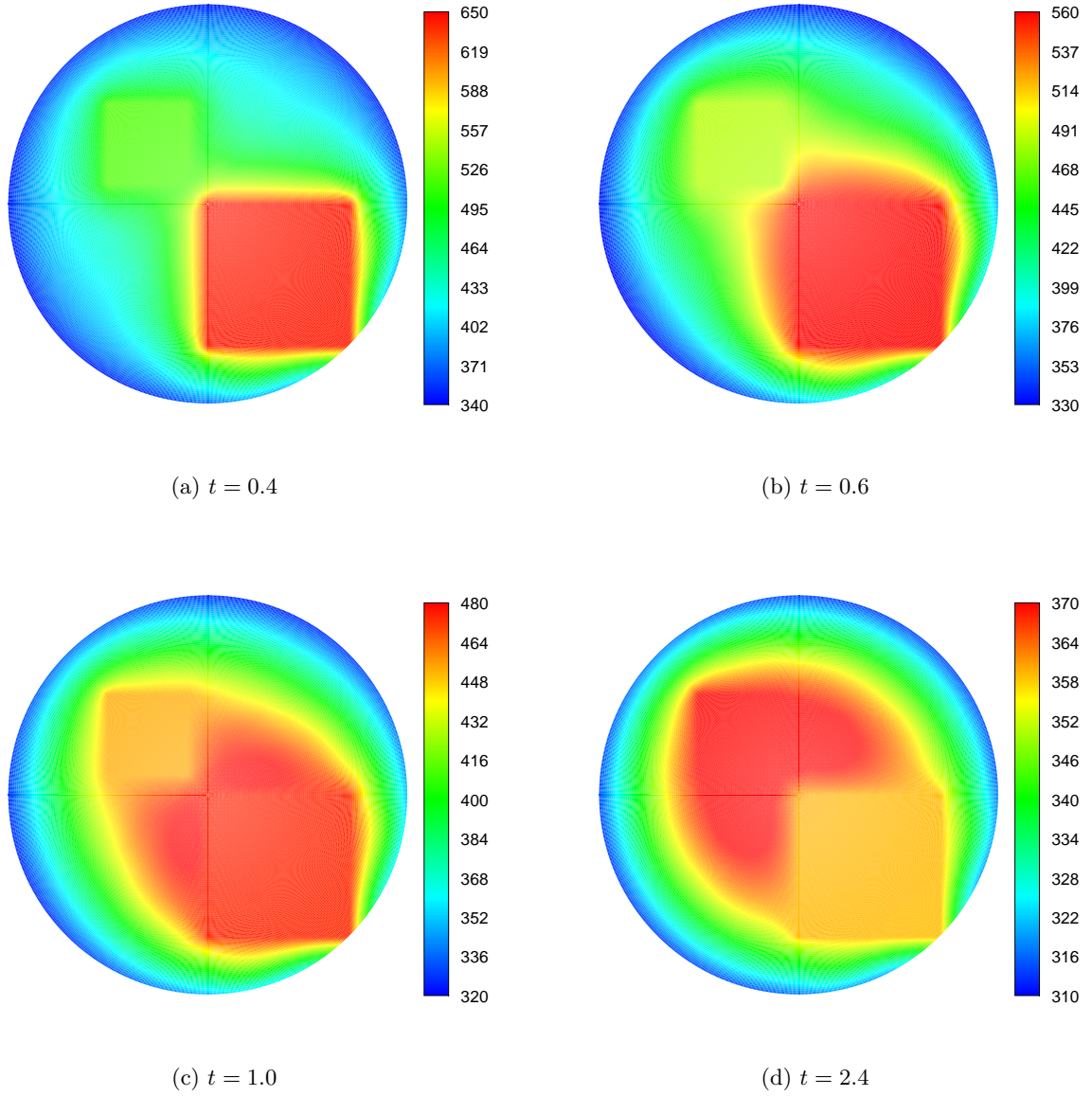


Figure 18: Temperature distribution obtained using the PUFEM for the test example of heat conduction in a composite with two inclusions as it cools down.

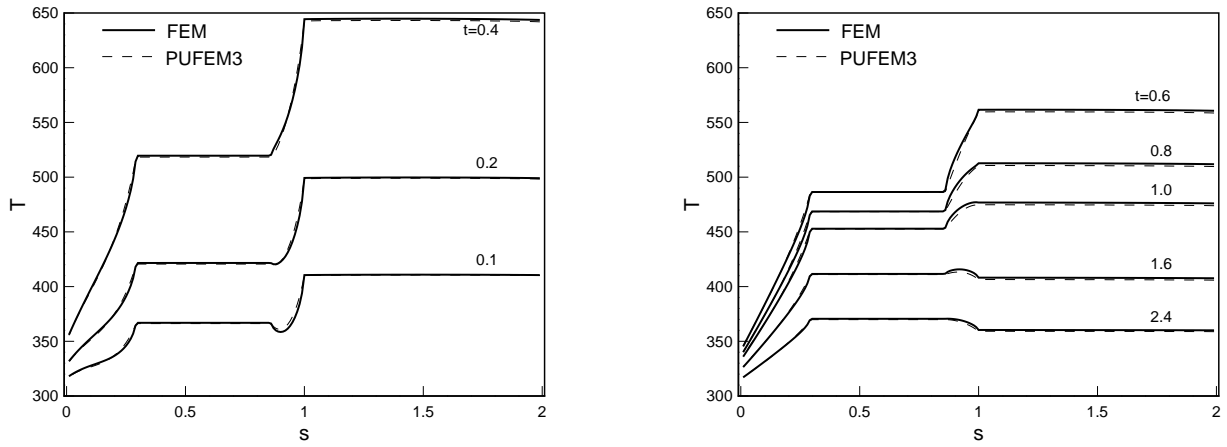


Figure 19: Cross sections of the temperature at the main diagonal passing through the points p_1 and p_2 shown in Figure 16. PUFEM3 and FEM results are presented at the warming-up phase (left) and the cooling-down phase (right).

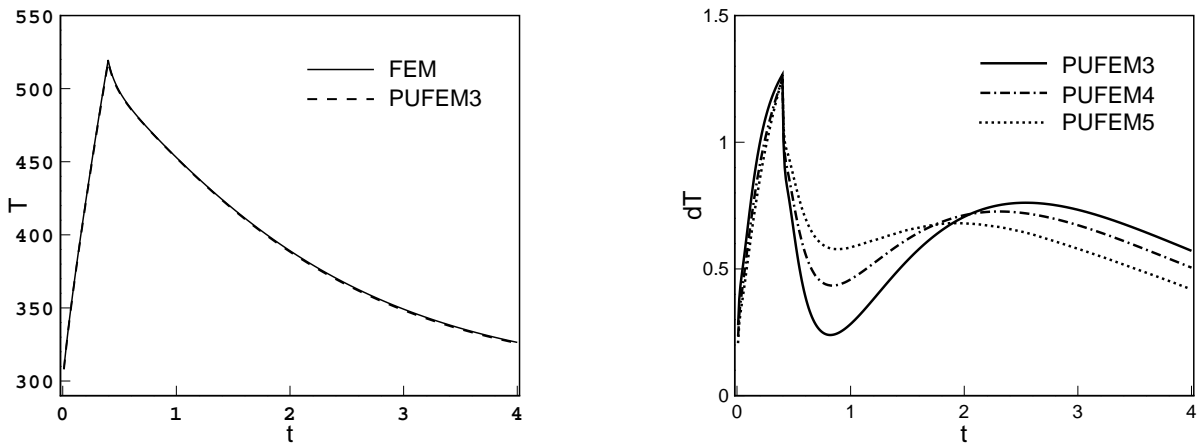


Figure 20: Time evolution of the temperature at the point p_1 (left) and time evolution of the temperature difference between the PUFEM and FEM at the point p_1 (right).

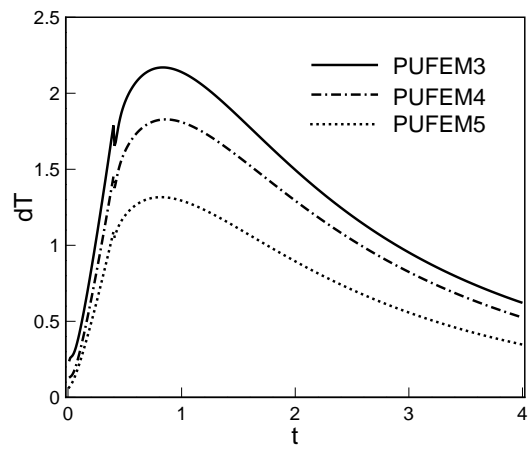
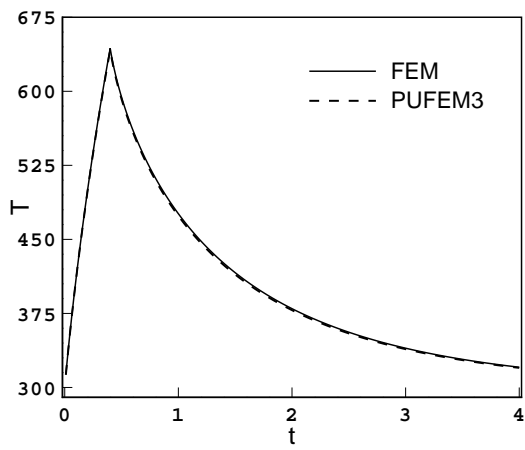


Figure 21: The same as Figure 20 but at the point p_2 .